

https://dspace.org/

Holographic measurement of the 26m HartRAO telescope

Klein, Benjamin

2009-05-08T10:08:02Z
http://hdl.handle.net/10539/6936

Downloaded from a DSpace repository. https://dspace.org/

Holographic Measurement of the 26m HartRAO Telescope

Benjamin Klein

A dissertation submitted to the Faculty of Engineering and the Built Environment, University of the Witwatersrand, Johannesburg, in fulfilment of the requirements for the degree of Master of Science in Engineering.

Johannesburg, 2008

Declaration

I declare that this dissertation is my own, unaided work, except where otherwise acknowledged. It is being submitted for the degree of Master of Science in Engineering in the University of the Witwatersrand, Johannesburg. It has not been submitted before for any degree or examination in any other university.

Signed this _____ day of _____ 20___

Benjamin Klein

Abstract

Microwave holography is a well established method of using the Fourier relationship between an antenna's current distribution and its complex beam-pattern to produce surface maps of large parabolic antennas. As the final part of a surface upgrade, a holographic map of the HartRAO 26 m telescope was produced. This showed that the surface has an RMS error of 0.45 mm. The measurement used a small reference dish to correlate against and retrieve amplitude and phase values. Due to system phase instabilities, this dish had to be attached to the measured antenna in order to enable sharing a high frequency local oscillator (LO). The movement was modelled and corrected for. However, a slight distortion remained. It is recommended that, either the LO distribution system is stabilised by using multiple PLLs or amplifiers and low loss cables are used to enable moving the reference antenna to a stationary position.

Acknowledgements

Without the support and love of my family none of this would be possible. You have helped me more than you will ever know.

To my supervisors Prof A. R. Clark, for the guidance and the space to find the solution, thank you. And to Dr. Jonathan Quick, for all the advice and assistance; it has been a privilege.

Additional thanks to Mike Kesteven, for generously giving his time in answering my many emails.

I would also like to thank the staff at Hartebeeshoek for helping me implement every crazy scheme with unwavering support. This project would have been impossible without you. To everyone in the workshop: Andre, Andrew, Attie, Lerato, Jacques, Keith, Piet, Pieter and Paul for drilling, milling, welding and letting me drive the cheery picker. To the research staff: Marion, Mike, Sarah and Sharmila for always leaving your door open. To the ground staff: Andrew, Ben, David, Joshua, Peter, Neels and Thomas for helping me move equipment and keeping everything running. To finance and admin: Katlego, Kedibon, Meisie, Simangele and Thea for keeping track of me. To Sam and Ronnie for the ping-pong, Glenda for allowing me to borrow her books; even if I never returned them. To all the students too numerous to name, for all the fun. To George for always listening. And finally I would like to thank Johanna and Sophy for the tea and cakes without which I might never have made it in on Mondays.

Preface

This dissertation is presented to the University of the Witwatersrand, Johannesburg for the degree of Master of Science in Engineering.

The dissertation is entitled *Holographic Measurement of the 26m HartRAO Telescope*

This document complies with the university's *paper model format*. The paper contains the main results of the research. The appendices present in detail the work conducted during the research.

Contents

Declaration i

Abstract ii

Acknowledgements iii

Preface iv

Contents v

List of Figures viii

List of Tables

I Introduction 1

II Holographic Theory 1

II-A Fundamentals 1

II-B Measurement Theory 2

II-C Simulations 2

III System 2

III-A Receiver 3

III-B Phase Stabilisation 3

III-C Modelled System phase 3

III-D Calibration 4

III-E Software 4

IV Source 4

IV-A Satellite Option 4

IV-A1 Tracking 4

V Results 4

VI Conclusions 6

References 6

A Holographic Measurement Theory **A.1**

A.1 Introduction A.1

A.2 Fourier Relationship A.1

A.3 Sampling Theory A.3

A.4 Correlation A.4

A.5 Simulations A.8

A.5.1 Phase error A.8

A.5.2 Current distribution A.9

A.6 Conclusions A.9

References A.10

B Holographic Physical System Considerations **B.1**

B.1 Introduction B.1

B.2 Receiver System B.2

B.2.1 HartRAO Dish B.2

B.2.2 Reference Dish B.5

B.2.3 IF components B.6

B.3 Oscillator distribution B.6

B.3.1 Phase Noise B.6

B.3.2 Phase Stabilisation B.7

B.4 Phase variation B.7

B.5 Calibration B.8

B.5.1 Amplitude B.9

B.5.2 Phase B.9

B.6 Software B.10

B.7 Conclusions B.10

References B.10

C Satellite Considerations **C.1**

C.1 Introduction C.1

C.2 Satellite Choices C.1

C.2.1 Requirements C.1

C.2.2 Satellite Option C.1

C.3 Technical considerations C.2

C.3.1 Tracking C.2

C.3.2 Received power C.4

C.4 Conclusions C.5

References C.5

D Hyperbolic derivation **D.1**

D.1 Introduction D.1

D.2 Derivation D.1

D.3 Conclusions D.4

References D.4

E Reference Antenna Mounting **E.1**

E.1 Introduction E.1

E.2 Calculation E.1

E.3 Conclusions E.4

References E.4

List of Figures

1 HartRAO telescope with attached reference dish 1

2 Equivalent geometry of a parabolic reflector 1

3 Panel map of HartRAO's parabolic reflector 2

4 Simulated holographic image 2

5 System diagram. 3

6 Main antenna geometry with attached reference dish 3

7 Holographic map showing surface distortions. 5

8 Final holographic map. 5

9 Histogram of measured errors across the aperture for each point in mm. 6

A.1 Equivalent geometry of a parabolic reflector A.1

A.2 Resolved area [m^2] and points per panel vs mapped points N. A.4

A.3 Plot of signal SNR vs. the RMS error A.4

A.4 Phase probability distributions A.5

A.5 Amplitude probability distributions A.6

A.6 Phase error probability A.6

A.7 Amplitude error probability A.7

A.8 Correlation time [s] vs resolvable surface error [mm] (N=64) A.7

A.9 Surface distortion geometry A.8

A.10 Simulated current distribution across the HarRAO dish. A.9

A.11 Simulated beam pattern A.10

A.12 Simulated holographic image A.10

B.1 System diagram. B.1

B.2 Geometry of cassegrain antenna B.2

B.3 Dual-mode potter horn. B.3

B.4 Dual-mode horn beam-pattern amplitude [dB] vs. angle [deg]. B.3

B.5 Hyperbolic reflector geometry B.4

B.6 Panel map of parabolic reflector B.4

B.7 Plots of simulated support structure blockage. B.5

B.8 Histogram of measured phase noise on a single PLL at 10.510 GHz B.7

B.9 Main antenna geometry with attached reference dish B.8

B.10 Bore-site phase data. B.9

C.1 Predicted movement of geostationary satellite C.3

C.2 Predicted movement of satellite Eutelsat W2 . . . . . C.3

C.3 Probability distribution of the error in NASA/NORAD model (dec plane) C.4

C.4 Probability distribution of the error in NASA/NORAD model (ha plane) C.4

D.1 Hyperbolic reflector orientation D.1

E.1 Geometry of antenna and satellite E.1

E.2 Hour angle and declination satellite look angles (un-tilted) E.2

E.3 Satellite look angles with tilted antenna E.3

E.4 Azimuth and elevation satellite look angles E.4

List of Tables

1 Satellite options arranged according to Hour Angle. 4

C.1 Satellite options arranged according to Hour Angle. C.2

Part 1

Paper: Holographic Measurement of the 26m HartRAO Telescope

Holographic Measurement of the 26m HartRAO Telescope

Benjamin Klein

***Abstract*—Microwave holography is a well established method of using the Fourier relationship between an antenna's current distribution and its complex beam-pattern to produce surface maps of large parabolic antennas. As the final part of a surface upgrade, a holographic map of the HartRAO 26 m telescope was produced. This showed that the surface has an RMS error of 0.45 mm. The measurement used a small reference dish to correlate against and retrieve amplitude and phase values. Due to system phase instabilities, this dish had to be attached to the measured antenna in order to enable sharing a high frequency local oscillator (LO). The movement was modelled and corrected for. However, a slight distortion remained. It is recommended that, either the LO distribution system is stabilised by using multiple PLLs or amplifiers and low loss cables are used to enable moving the reference antenna to a stationary position.**

***Index Terms*—Holography, microwave, phase-stabilisation.**

I. Introduction

The holographic measurement of the Hartebeesthoek Radio Astronomy Observatory's (HartRAO) telescope is the final phase of a surface upgrade to enable research at higher frequencies, specifically the 22 GHz water line. This translates roughly to removing surface errors greater than $^1/_2$ mm. The project began in 1998 replacing previously perforated panels with solid ones. The panels have been mounted and aligned mechanically using a theodolite. For long term operation and periodic monitoring an indirect method is needed. Microwave holographic is a logical choice having been applied successfully to many antennas: Effelsburg 100m antenna 1986, 64 m NASA/JPL 1984-85, 34 m and 70 m DSN antennas 1992, 32 m Medicina radio-telescope 1993 etc. [1], [2], [3]. Microwave holography is a measurement technique founded on the well established Fourier transform relationship between an antenna's complex beam pattern and its current distribution [4], [5] - which in turn directly relates to the antenna's surface. The holographic technique was originally developed at the University of Sheffield [6]. In 1985 *Rahmat-Samii* formalised a method for determining the relationship between the surface errors and the aperture phase [1], [7]. (Errors introduced by the measurement are categorised by *Rochblatt* and *Rahmat-Samii* [8], [2]). The main antenna is a cassegrain reflector consisting of a 26 m parabolic reflector and a 3 m hyperbolic reflector, the system is shown in figure 1. The measurement is performed by scanning the HartRAO telescope, in a square raster pattern, across a strong source (a geostationary satellite). The measured signal is cross-correlated with a stationary signal obtained from a reference antenna — typically a small (≈ 0.5 m) offset parabola. Producing a square grid of points sampling the complex antenna far-field radiation or beam pattern. The measured surface accuracy is directly dependent on the phase and amplitude stability of the system. The following document outlines the theory; details the specific application and presents results, conclusions and recommendations.

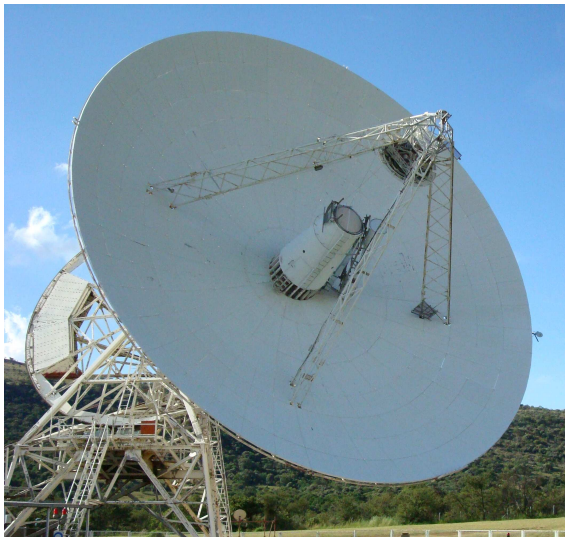


Fig. 1. HartRAO telescope with attached reference dish.

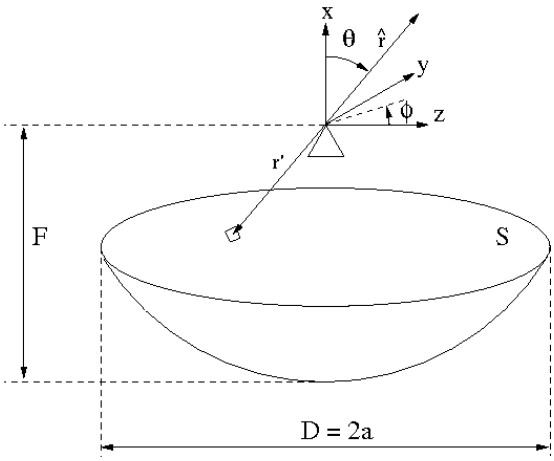


Fig. 2. Equivalent geometry of a parabolic reflector (adapted from [1]).

II. Holographic Theory

The following theory is based primarily on work by *Rochblatt* and *Rahmat-Samii* [2], [1]. The theory is summarised here, details are presented in [9] appendix A.

A. Fundamentals

Microwave holography is a measurement technique founded on the mathematical relationship between current distribution ($\mathbf{J}$) and the antenna beam pattern ($\mathbf{T}$) [4], [5]. Under a small observational angle assumption this simplifies to the Fourier relationship (referring to figure 2):

$$\mathbf{T}(u,v) = \int\int_S \mathbf{J}(x',y')e^{jkz'} e^{jk(ux'+vy')}dx'dy' \quad (1)$$

where:

$z'(x',y')$:	Dish surface S
u,v :	Cosine space

The required surface error function $\varepsilon(x,y)$ is related to the measured antenna beam pattern using a geometrical ray tracing argument [7]:

$$\varepsilon(x,y) = \frac{\lambda}{4\pi}\sqrt{1+\frac{x^2+y^2}{4F^2}}\angle\{e^{j2kF}\mathscr{F}^{-1}[\mathbf{T}(u,v)]\} \quad (2)$$

where:

F :	Dish focal length
λ :	Source wavelength

Consequently by measuring the beam pattern, in both phase and amplitude, the surface error profile can be reconstructed.

B. Measurement Theory

The measurement is performed in a raster of discrete points N × N. Equation 1 is computed in the following discritized form:

$$\mathbf{T}(p\Delta u, q\Delta v) = sxsy\sum_{n=\frac{N}{2}}^{\frac{N}{2}-1}\sum_{m=\frac{N}{2}}^{\frac{N}{2}-1}\mathbf{J}(nsx,nsy) e^{j2\pi(\frac{np+mq}{N})} \quad (3)$$

Where n, m, p, q are the integers indexing the discrete samples, $\Delta u, \Delta v$ are the sampling intervals in cosine space (beam coordinates) and sx, sy the interval aperture space (antenna surface coordinates), calculated as:

$$\Delta u = \Delta v = \frac{k\lambda}{D} \quad (4)$$

$$sx = sy = \frac{D}{kN} \quad (5)$$

Where k is the oversampling factor $0.5 < k < 1$. The nyquist sampling interval for an antenna of diameter D_λ in wavelength is given by ${D_\lambda}^{-1}$ [10]. Sampling finer than a factor of 0.7 improves the map little [11]. The HartRAO map was sampled at 0.75 giving an angular distance of 0.0425° between the points. The resolved limit of the map ϵ, dependant on the signal to noise ratio (SNR), is derived in [9] appendix A (based on the work done by *Butler* [12]) as:

$$\epsilon_{err} \approx \frac{\lambda N}{3.4\pi \mathrm{SNR}} \quad (6)$$

and consequential spatial resolution δ:

$$\delta = \frac{D}{kN} \quad (7)$$

The HartRAO telescope consists of 252 discrete panels (shown in figure 3), connected to the backing structure of the main telescope. Each panel is a rigid shape with adjustment screws (four or more) allowing the panel to be raised, lowered and tilted. The required spatial resolution is dependant on the size of the panel elements. A minimum of three and a recommended four points are required, per panel, to determine the correction required. The theoretically resolvable error is $\epsilon_{err} < 0.1$ mm.

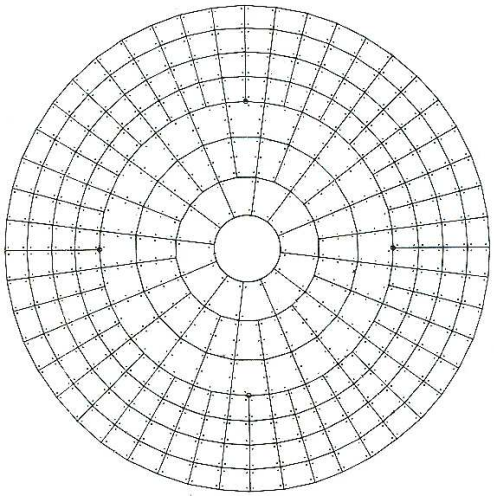


Fig. 3. Panel map of HartRAO's parabolic reflector, shown with associated adjustment screws.

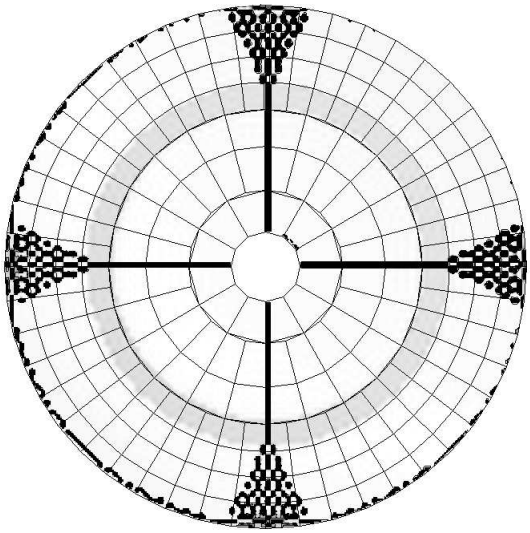


Fig. 4. Simulated holographic image produced from a generated beam pattern of a 26 m parabolic antenna with a ring of panels displaced by 0.5 mm, (blockage pattern is included).

C. Simulations

In order to test the theory and software reduction system, simulations of the map were required. Surface distortions are simulated by specifying the error function ε in equation 2 and solving for ($\mathbf{T}$). The resultant beam pattern was used to test the analysis software by recovering the ε function. Noise and systematic errors are included to give an idea of the effect on the accuracy of the final measurement. The simulated pattern of a ring of distorted panels is plotted in figure 4. The map is sized to correspond with the minimum measured raster size of 64×64.

III. System

Full details of the receiver system are presented in [9] appendix B.

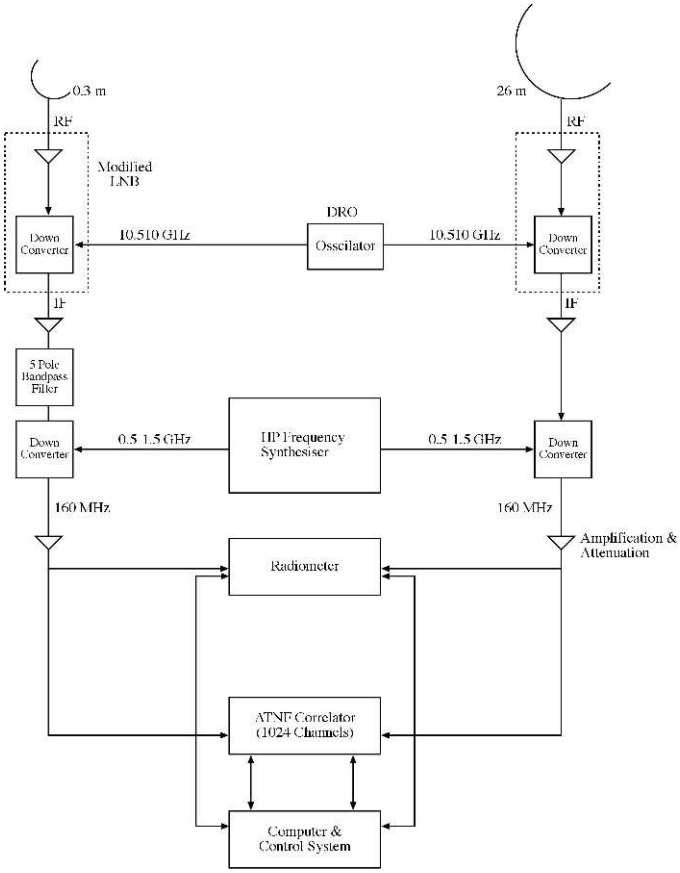


Fig. 5. System diagram.

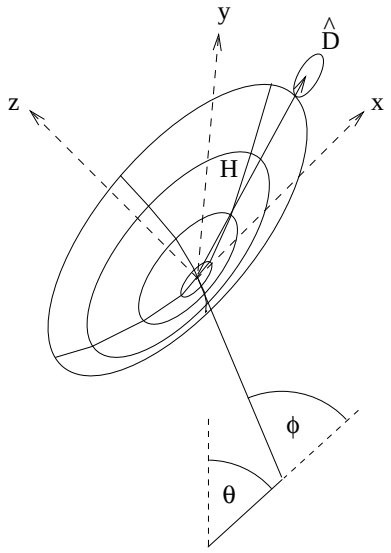


Fig. 6. Main antenna geometry with attached reference dish.

A. Receiver

The system is a two element interferometer consisting of a 26 m diameter telescope (to be measured) and, attached to it a 0.3 m reference antenna. An overview of the system is given in figure 5. The HartRAO telescope consists of multiple switchable systems. Each system down converts its RF into the central range of the general intermediate frequency (IF) system ≈ 1.5 GHz and then a common system down converts further to 160 MHz (for transmission down to the ground and analysis). Consequently two mixer stages are required, one for each down conversion, for the holographic system a 10.510 GHz oscillator is used for the first down conversion. Each down conversion involves a local oscillator (LO). Special care must be taken to avoid introducing phase noise from these oscillators.

B. Phase Stabilisation

Phase instabilities translate directly to measurement errors by a factor $^{\lambda}/_{2\pi}$. Tolerance of 0.1 mm results in a phase tolerance, at 12 GHz, of $\approx 2^{\circ}$. Systematic errors are of primary concern. Purely random errors average out in both the correlation and in the Fourier integral. Simulations showed that random errors of less than $\approx 10^{\circ}$ are acceptable.

a) Current System: The HartRAO system uses a single phase-locked loop (PLL) system to stabilise the millimetre oscillators used in down conversion. Phase noise requirements for single dish observations are relatively low. Phase closure is used to achieve higher stability for Very Long Baseline Interferometry (VLBI) [10]. As a result the HartRAO telescope has a simple phase distribution system. A highly stable low-noise 5 MHz signal is generated using an Atomic Maser, which is cabled to a series of LOs and phase-locked using a PLL. The cables are calibrated using a delayed 1 ms 5 MHz pulse sent down a similar cable [13].

b) Measured Noise: Phase noise is linearly dependant on the frequency of the oscillator and the HF sections of the system are principally considered [14]. The locking signals, although low frequency, are considered part of the HF system as any phase noise within them is multiplied up linearly by the PLL. The system consists of matched left circularly polarised (LCP) and right circularly polarised (RCP) chains, which are correlated against each other to measure the inherent phase noise in the IF system. The system's phase noise, without the LO circuitry, is measured at below 1°. The LO distribution phase noise, (measured using a synthesised test signal), is $\approx 16^{\circ}$ with an associated drift. This is too high for the desired map and would not measure the surface to the required accuracy.

c) Stabilisation Schemes: To achieve the high levels of phase stability in the LO distribution a series of PLL loops are required. Typical applications are given by *Legg* [15] and *Little* [16]. This was not possible given time and budget constraints. In order to overcome the higher frequency instabilities the two systems, instead of using a PLL, shared a common LO via a short connector. The configuration required physically connecting the two dishes. This adds to the complexity of the reference antenna moving with the main antenna, but it stabilised the overall phase noise to 5° and removed high drift rates.

C. Modelled System phase

Attaching the reference dish to the antenna structure, introduces a phase variation, resulting from a differential movement of the phase centres of the antennas. This is calculated and corrected for. The phase variation is a result of changing the distance (H) between the two feeds and the satellite source. Referring to figure 6, the distance H, is calculated as:

$$\begin{aligned} H =& \mathbf{z} \cdot R_x R_y \begin{pmatrix} D_x \\ D_y \\ D_z \end{pmatrix} = \mathbf{z} \cdot \begin{pmatrix} 1 & 0 & 0 \\ 0 & \cos\phi & \sin\phi \\ 0 & \sin\phi & \cos\phi \end{pmatrix} \times \\ & \begin{pmatrix} \cos\theta & 0 & -\sin\theta \\ 0 & 1 & 0 \\ \sin\theta & 0 & \cos\theta \end{pmatrix} \begin{pmatrix} D_x \\ D_y \\ D_z \end{pmatrix} \\ =& D_y \sin\phi + D_z \cos\theta \cos\phi \end{aligned} \tag{8}$$

where R_x and R_y are general rotation matrices [17].

D. Calibration

The measurement is referenced to the central point of the map (the bore-site), as the length of the measurement can be significant, in order to resolve out drifts this point needs to be re-measured periodically (every few hours). Unlike astronomical measurements however, holography does not need to resolve absolute amplitudes but relative amplitudes.

d) Amplitude: The astronomical receiver is calibrated using a variation on the standard noise diode method [18]. Typically, in radio astronomy, the receiver level is measured by turning on a noise diode and injecting its signal into the waveguide as close to the feed as possible. To obtain the systems zero level a standard $50\ \Omega$ load is used at the input to the detector. The measured amplitude is zeroed and scaled by the know value of the diode. In the holographic system, the reference dish has no noise diode and instead its auto-correlation is measured and used to track gain variations in the system. A radiometer is used to measure the total power of both channels and track system temperature changes. The cross correlation is scaled using automatic gain control (AGC) and recorded as a raw, dimensionless quantity. The data is calibrated to a meaningful value by scaling it by the system temperature to convert it to Kelvins. The system temperature is the ratio between the total power recorded TP (in Hz) and the noised diode calibrator recorded H in Hz/K. The calibrated auto-correlation A is given in equation 9 and the calibrated cross-correlation C in equation 10.

$$A = A_{\text{meas}} \frac{TP_{\text{R}}}{H_{\text{R}}} \tag{9}$$

$$C = C_{\text{meas}} \sqrt{\frac{TP_{\text{M}} TP_{\text{R}}}{H_{\text{M}} H_{\text{R}}}} \tag{10}$$

Where, A_{meas} and C_{meas} are the measured values directly from the correlator and the M and R subscripts indicate the main and reference system respectively. In order to obtain a measured power of the antenna's gain M_{gain}, independent of variations in the satellite strength and reference antenna gain, the calibrated cross-correlation C must be divided by the square root of the auto-correlation A, as follows (shown in equation 11):

$$M_{\text{gain}} = C_{\text{meas}} \sqrt{\frac{TP_{\text{M}}}{A_{\text{meas}} H_{\text{M}}}} \tag{11}$$

The M_{gain} is in volts. The final gain is independent of the reference dish's system temperature as expected.

e) Phase: Phase calibration is done periodically (≈ 30 minutes) on the bore-site and variations during the measurements are modelled out. The phase drift must, consequently, be close to linear during the measurement and lower than a 180° rate per bore-site in order to resolve out phase wrapping. Measurements showed that the rate was slow enough.

E. Software

The data is recorded into the standard format FITS [19] and later reduced using custom routines, written using the mathematical package, Octave [20]. The Fourier transform is calculated and the images are produced using the Astronomical Image Processing System (AIPS) [21] and Miriad packages [22]. The specific routine is detailed by *Graves* and *Kesteven* [23].

Table 1
SATELLITE OPTIONS ARRANGED ACCORDING TO HOUR ANGLE.

Satellite Name	Long-itude	Hour Angle [deg]	Beacon Frequency [GHz]
Bonum 1	56	32.51	11.706
Europe Star 1	45	19.98	11.697
Eurasiasat 1	42	16.53	11.699
Eutelsat Sesat	36	9.62	11.450
Eutelsat W4	36	9.62	11.706
Eurobird	28.2	0.6	11.200
Astra 1B	19.2	-9.81	11.697
Eutelsat W2	16	-13.51	11.698
Hot Bird 5	13	-16.96	11.699
Eutelsat W1	10	-20.4	11.451
Eutelsat W3	7	-23.84	12.501
Sirius 2	5	-26.11	11.777

IV. SOURCE

Geostationary satellites are high power, stable and still sources and therefore ideally suited for holographic measurements. The systems gain is very high ≈ 67 dB and to avoid saturation the broad-band carrier is filtered out and a continuous wave (CW) locking beacon is used instead for correlation. Note, in the case of low gain, it is possible to use the broad-band carrier for holography if the associated lags across the correlator are corrected for.

A. Satellite Option

To locate available satellites a media search and a power scan on the sky was done. The usable satellites are given in table 1. The optimum satellite for HartRAO is Eutelsat W2.

1) Tracking: Geostationary satellites, although highly stable, drift appreciably within the beam of the telescope (HPBW $\approx 0.059^\circ$) and need to be actively tracked. The model used is the Keplerian elements implemented using the NASA/NORAD format provided by CelesTrak [24]. NORAD does not return the accuracy of the prediction, however, it is possible to estimate the deviation of the prediction over time using the model itself [25]. By comparing an older ephemeris with a more recent one the stability or the speed at which the model degrades is measured. Simulations show that over the modelled period, approximately three days for Eutelsat W2, this varied by $\approx 0.03^\circ$. This is removed by performing periodic cross scans across the source during the map and calculating the offset.

V. RESULTS

The final holographic map was recorded at night, several hours after the sun had set. This provided as temperature stable a measurement as possible. Three panels were deliberately displaced, (one raised 6 mm, one raised 2 mm and one lowered 6 mm) in order to test the measurement. The results are plotted in figure 7. The map is produced with $N = 80$ and an oversampling factor of $k = 0.76$. The map shows that the dish's accuracy is set within a millimetre of an ideal surface. The distortion present in the southern area of the dish is gravitational sagging and, as the dish is equatorial mounted, cannot be improved. The purposefully displaced panels are clearly visible and correctly measured. The panel map grid is misaligned, applying the mathematical correction discussed in section III-C largely corrects it and the result is plotted in figure 8.

The measured root mean square (RMS) distortion of the surface is 0.45 mm, the fitted histogram is plotted in figure 9.

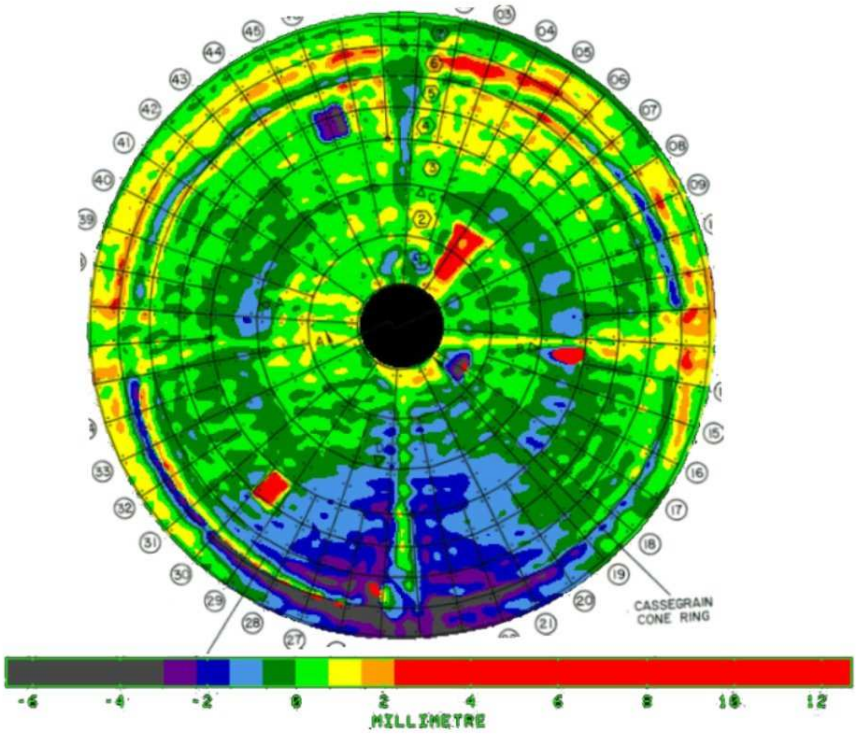


Fig. 7. Holographic map showing surface distortions.

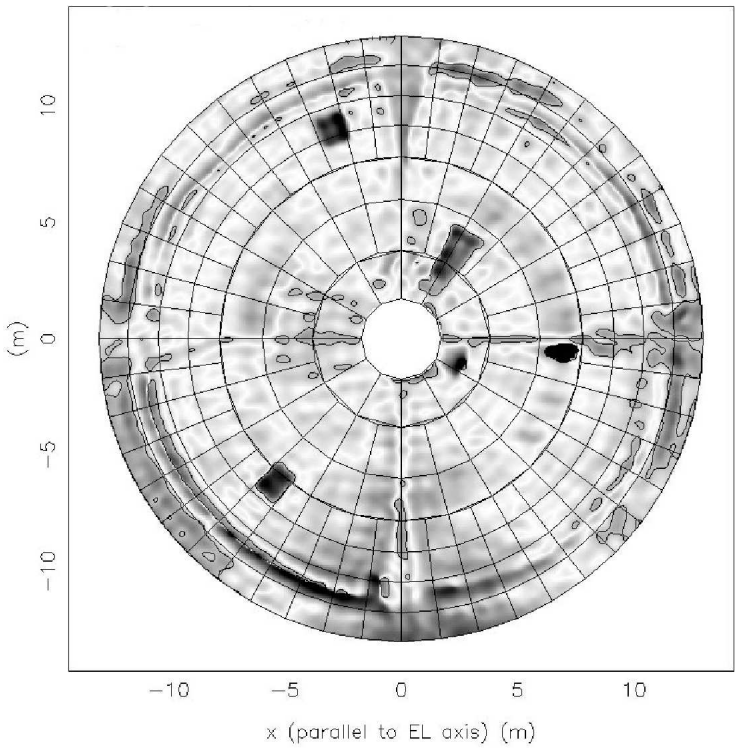


Fig. 8. Final holographic map.

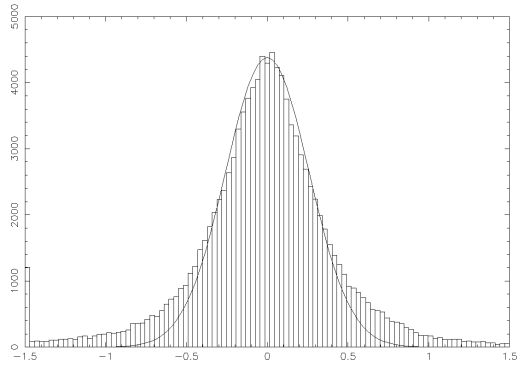


Fig. 9. Histogram of measured errors across the aperture for each point in mm.

VI. Conclusions

The holographic measurement system worked correctly and, along with the chosen satellite Eutelsat W2, provided the required stability for the map. The band-pass filter and system alterations worked correctly, allowing the low power receivers to be adapted to work with a strong source. The overall system does not impact the normal operation of the telescope and is configured so as to allow remote operation (without any manual hardware switching). This, along with the method of scanning the telescope, allows a map to be broken up and slotted into the observing schedule. The overall map took eight to ten hours, short enough to be scheduled every few months and used for routine monitering of the dish surface. The correlation and mathematical reduction software was tested and worked correctly. The resulting map, given the size and spacing, is resolved as expected and the structure of the dish is clearly visible. Residual distortions within the map are slight, but still present problems determining individual panel corrections. To correct for this the reference dish should be moved such that it does not move with the main antenna, achievable in two ways. By stabilising the oscillator distribution system or using high frequency amplifiers and waveguide to still enable sharing the first LO. The dish is measured to have an RMS accuracy of 0.45 mm, sufficient to allow it perform 22 GHz research.

References

[1] Y. Rahmat-Samii. Surface diagnosis of large reflector antenna using microwave holographic metrology: An iterative approach. *Radio Science*, 19(5):1205–1217, September-October 1984.

[2] David J. Rochblatt. Microwave antenna holography. *IEEE Transactions on Microwave Theory and Technique*, 40(6):1294–1300, June 1992.

[3] D. Tarchi and G. Comoretto. Holographic measurement on Medicina radio telescope using artificial satellites at 11 GHz. *Astronomy and Astrophysics*, 275:679–685, April 1993.

[4] S. Silver. *Microwave Antenna Theory and Design*. McGraw-Hill Book Company, INC., 1949.

[5] John D. Kraus. *Antennas*. McGraw-Hill Book Company, INC., New York, Toronto, London, August 1950.

[6] A. P. Anderson J. C. Bennett, Peter A. McInnes, and A. J. Whitaker. Microwave holographic metrology of large reflector antennas. *IEEE Transactions on Antennas and Propagation*, AP-24(3):295–303, May 1976.

[7] Yahya Rahmat-Samii. Microwave holography of large reflector antennas-simulation algorithms. *IEEE Transactions on Antennas and Propagation*, AP-33(11):1194–1203, November 1985.

[8] Rochblatt David J and Yahya Rahmat-Samii. Effects of measurement errors on microwave antenna holography. *IEEE Transactions on Antennas and Propagation*, 39(7):933–942, July 1991. 1991.

[9] Benjamin Klein. Holographic measurement of the 26m hartrao telescope. Master's thesis, School of Electrical Enginnering, University of the Witwatersrand, Johannesburg, 2008.

[10] A. Richard Thomson, James M. Moran, and JR. George W. Swenson. *Interferometry and Synthesis in Radio Radio Astronomy*. John Wiley and Sons, New York, Chichester, Brisbane, Toronto and Singapore, 1986.

[11] Bryan Butler. Simulations of some types of holography errors for vlba antennas. Technical report, National Radio Astronomy Observatory, April 1999. VLBA Test Memo. No. 62.

[12] Bryan Butler. Options for VLBA Antenna Surface Measurement. Technical report, National Radio Astronomy Observatory, March 1998. VLBA Test Memo. No. 57.

[13] Alan E.E. Rogers. *Manual for Mark III Phase and Group Delay Calibraor*. Haystack Observatory.

[14] Jussi Saily. *Instrumentation of Submillimetre Wave Hologram Compact Antenna Test Range*. Thesis for degree of doctor of science in technology, Helsinki University of Technology, September 2003.

[15] T. H. Legg. Microwave phase comparators for large antenna arrays. *IEEE Transactions on Antennas and Propagation*, 1964.

[16] Alec G. Little. A phase-measuring scheme for a large radiotelescope. *IEEE Transactions on Antennas and Propagation*, Ap-17(5), September 1969.

[17] Eric W Weisstein. Rotation matrix. From MathWorld–A Wolfram Web Resource. http://mathworld.wolfram.com/RotationMatrix.html. Last visited June 2007.

[18] M. Kesteven, D. Grahamn, O. Lochner E. Fürst, and J. Neidhöfer. The Effelsburg Holography Campaign -2001. Max-Planck-Institut für Radioastronomie, October 2001.

[19] Fits the astronomical image and table format. http://fits.gsfc.nasa.gov/. Last visited June 2007.

[20] Gnu octave. http://www.gnu.org/software/octave/. Last visited June 2007.

[21] NRAO. Astronomical image processing system. http://www.aips.nrao.edu/. Last visited June 2007.

[22] Australian Telescope National Facility. Miriad. http://www.atnf.csiro.au/computing/software/miriad/. Last visited June 2007.

[23] G. Graves and M. Kesteven. Compact array holography. AT documentation, June 1995.

[24] Dr. T.S. Kelso. Celestrak. http://celestrak.com/. Last visited June 2007.

[25] Dr. T.S. Kelso. More frequently asked questions. Satellite Times online at http://celestrak.com/columns/v04n05/index.asp#FAQ06, May 1998. Last visited June 2007.

Part 2

Appendices

Appendix A

Holographic Measurement Theory

A.1 Introduction

The holographic technique was originally developed at the University of Sheffield in 1976 [1], the first application to a large reflector antenna was done at the Mullard Radio Astronomy Observatory in 1977 [2]. The theory is based on well established Fourier transform relationship between an antenna's complex beam pattern and its current distribution [3], [4] - which in turn directly relates to the antenna's surface. The image is produced by computing the resulting 2-dimensional Fourier transform. In 1985 *Rahmat-Samii* formalised a method for determining the relationship between the surface errors and the aperture phase [5], [6]. The theory is well established and understood. An overview and summary is given here, with paticular ephasis on the measurment theory and the relationship with the source's Signal to Noise Ratio (SNR). The specific measurment method of cross-correlation is presented and linked with the sampling and error theory. Based on the theory the measurement is simulated and tested using reduction software.

A.2 Fourier Relationship

The following theory is based on the discussion by *Rahmat-Sammii* as presented in [5]; on the Fourier relationship between the surface current and the far field radiation pattern. The geometry of the reflector and coordinate systems used are given in figure A.1.

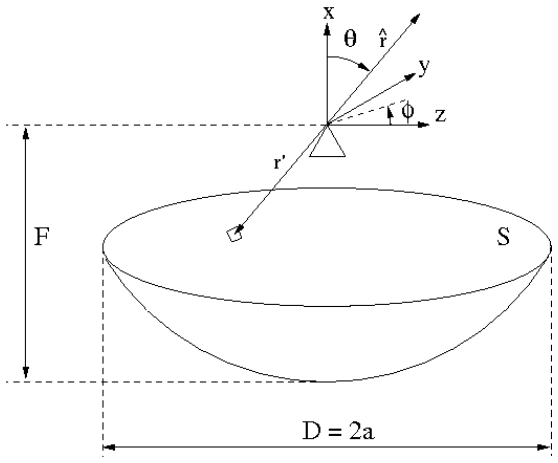


Figure A.1: Equivalent geometry of a parabolic reflector (adapted from [5]).

Using physical optics the radiation pattern can be expressed generally as:

$$\mathbf{E} = -jk\eta\frac{e^{-}jkr}{4\pi r}\left(T_\theta\hat{\theta} + T_\phi\hat{\phi}\right) \tag{A.1}$$

where **T** is the beam pattern, η is the free space impedance and $k = 2\pi/\lambda$. Using the physical optics integral this is expressed as:

$$\mathbf{T}(\theta,\phi) = \int_s \mathbf{J}(\mathbf{r}')e^{jk\mathbf{r}'\cdot\hat{\mathbf{r}}}dS' \tag{A.2}$$

where **J** is the induced surface current across the reflector (with unit normal **n**) defined as:

$$\mathbf{J} = 2\mathbf{n}\times\mathbf{H}' \tag{A.3}$$

Rahmat-Samii and *Galindo-Israel* [7] have shown how integral A.2 can be expressed across the aperture rather than the surface, using the surface Jacobian transformation:

$$\mathbf{J}_s = \sqrt{1 + \left(\frac{\partial f}{\partial x'}\right)^2 + \left(\frac{\partial f}{\partial y'}\right)^2} \tag{A.4}$$

into:

$$\mathbf{T}(\theta,\phi) = \int_s \mathbf{J}(\mathbf{r}')e^{jk\mathbf{r}'\cdot\hat{\mathbf{r}}}J_s dx'dy' \tag{A.5}$$

where $f = z'(x',y')$, the equation of the aperture. Note, that the current is still evaluated on the surface of the reflector not in the aperture plane.
Equation A.5 expresses a Fourier relationship for flat surfaces i.e z is a constant. This can be extended for the limited case of small observation angles θ (the case for electrically large reflectors). Using the following identities:

$$\mathbf{J}(x',y') = \mathbf{J}(\mathbf{r}')J_s \tag{A.6}$$
$$\mathbf{r}'\cdot\hat{\mathbf{r}} = z'\cos\theta + ux' + vy' \tag{A.7}$$
$$u = \sin\theta\cos\phi \tag{A.8}$$
$$v = \sin\theta\sin\phi \tag{A.9}$$

equation A.5 is simplified to gives the familiar Fourier relationship [3], [4]:

$$\mathbf{T}(u,v) = \int\int_S \mathbf{J}(x',y')e^{jkz'}e^{jk(ux'+vy')}dx'dy' \tag{A.10}$$

This is the dominant term in a Taylor expansion and only valid for small angles and undisplaced feeds, for these other cases the reader is referred to [7].

A.3 Sampling Theory

Equation A.10 is computed by sampling an N by N grid and solving the following sum:

$$\mathbf{T}(p\Delta u, q\Delta v) = sxsy \sum_{n=\frac{N}{2}}^{\frac{N}{2}-1} \sum_{m=\frac{N}{2}}^{\frac{N}{2}-1} \mathbf{J}(nsx, nsy) e^{j2\pi(\frac{np+mq}{N})} \tag{A.11}$$

where n, m, p, q are the integers indexing the discrete samples, $\Delta u, \Delta v$ are the sampling interval in u, v far field space, sx, sy is the sampling interval in the aperture space [8]. N is the size of the map. The sampling required is calculated using an adaption of the work done by *Butler* [9]. Using non phase-retrieval methods the aperture measurement error is given by:

$$\epsilon_{err}^{a} = \frac{\lambda}{2\pi}\psi_{err} \tag{A.12}$$

where ψ_{err} is the phase error in the aperture plane. In the case of a beacon signal with a high SNR (as measured at the centre of the map) this is:

$$\psi_{err} = \frac{N}{SNR} \tag{A.13}$$

The surface error is related to the aperture error as follows:

$$\epsilon_{err}^{s} = \frac{\epsilon_{err}^{a}}{2\cos(\gamma/2)} \tag{A.14}$$

where γ is the angle formed between the feed, sub-reflector and main reflector. Consequently the maximum error occurs at the edge of the dish at an angle of around $\gamma \sim 65^{\circ}$

$$\epsilon_{err}^{sedge} \sim \frac{\epsilon_{err}^{a}}{1.7} \tag{A.15}$$

Substituting equations A.15 and A.13 into equation A.12 gives the measurable error:

$$\epsilon_{err} \sim \frac{\lambda N}{3.4\pi \mathrm{SNR}} \tag{A.16}$$

The spatial resolution of the map δ is given as:

$$\delta = \frac{D}{kN} \tag{A.17}$$

where $0.5 < k < 1$ represents the oversampling factor of the map and D is the diameter of the dish. The critical sampling factor is $k = \frac{N}{N+1}$, the measurement averages errors over the integration and increasing the over sampling improves the map little [10]. Typically $0.7 < k < 0.8$ is sufficient. The resolved area per point is plotted with the number of points per panels in figure A.2.

Equation A.16 is rearranged to solve for the required SNR in terms of the desired antenna parameters by substituting equation A.17,

$$\mathrm{SNR} = \frac{\lambda D}{3.4\pi k \delta \epsilon_{err}} \tag{A.18}$$

The required SNR is plotted in figure A.3. Increasing the map size reduces the size of the resolved pixel within the map, i.e creates a sharper image, however, as seen from figure A.3, this reduces the accuracy

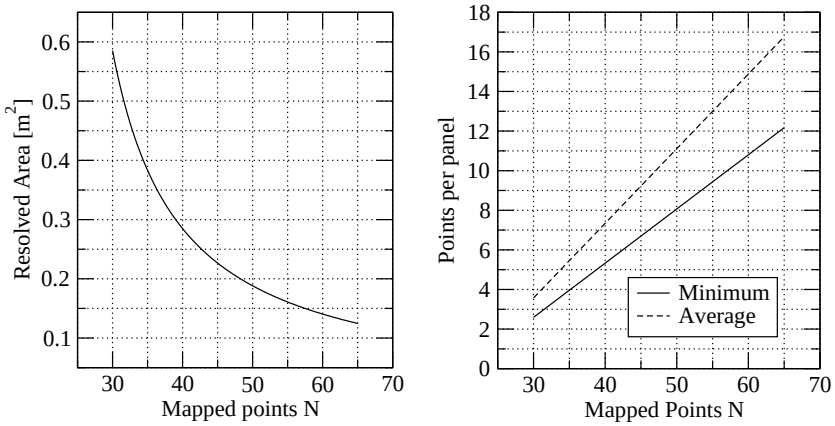


Figure A.2: Resolved area [m^2] and points per panel vs mapped points N.

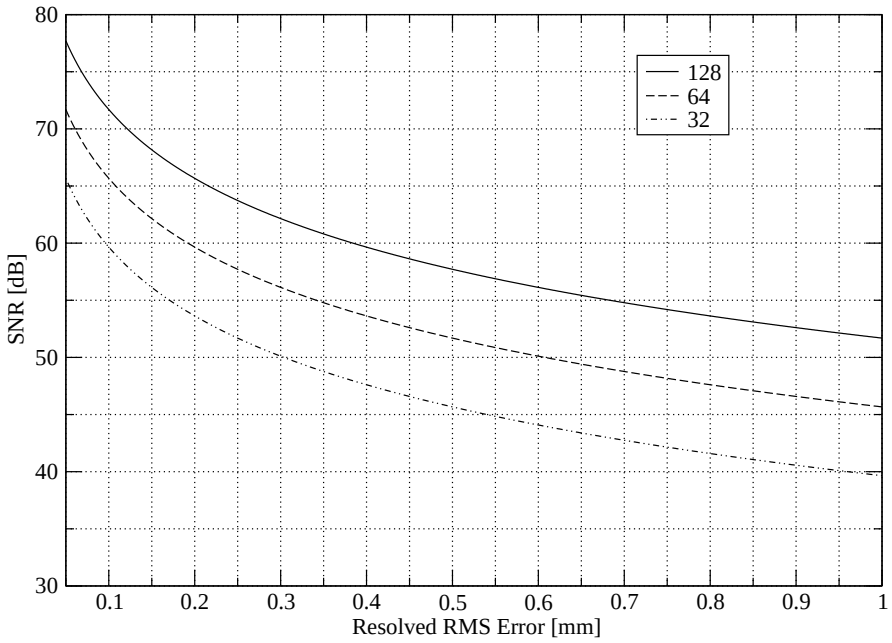


Figure A.3: Plot of signal SNR vs. the RMS error across the surface for the 26 m HartRAO telescope for various map sizes.

of the individual pixels (this can be understood as larger pixels cover a larger surface area and average out errors). Additional points map the beam to further out side-lobes and consequently require higher SNR in order for the added data to be meaningful.

A.4 Correlation

To obtain the phase difference and amplitude ratio, the signals from the reference and measured dishes, (the corresponding voltage vectors) must be mixed - the common method is cross-correlation [11]. The major advantage of this method is a reduction of noise due to local noise sources being filtered out, a requirement as the side lobes provide the highest resolution of the surface errors [12].

The cross-correlation of two monochromatic waves, is defined as [11]:

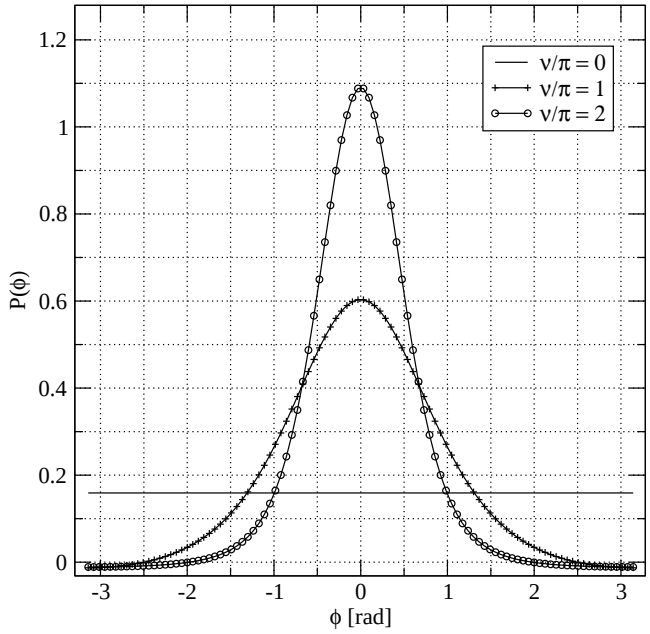


Figure A.4: Phase probability distributions

$$x(t) = E_x \sin(2\pi\omega t + \delta_x)$$
$$y(t) = E_y \sin(2\pi\omega t + \delta_y)$$

and solved as follows [13]:

$$\begin{aligned}\langle x(t)y(t)\rangle &= E_x E_y \lim_{T\to\infty}\int_{-T}^{T} \sin(2\pi\omega t + \delta_x)\sin(2\pi\omega t + \delta_y)\mathrm{d}t \\ &= E_x E_y \left(\frac{1}{2}\cos(\delta_x - \delta_y) - \lim_{T\to\infty}\int_{-T}^{T}\frac{1}{2}\cos(4\pi\omega t + \delta_x + \delta_y)\mathrm{d}t\right) \\ &= E_x E_y \cos(\delta_x - \delta_y)\end{aligned} \tag{A.19}$$

The probability distribution in the measured noise, in amplitude and phase, is [14].

$$P(A) = \frac{A}{\sigma^2} e^{-\frac{A^2+|\mathscr{V}|^2}{2\sigma^2}} I_o\left(\frac{A|\mathscr{V}|}{\sigma^2}\right) \tag{A.20}$$

$$P(\phi) = \frac{1}{2\pi} e^{-\frac{|\mathscr{V}|^2}{2\sigma^2}} \left(1 + \sqrt{\frac{\pi}{2}}\frac{|\mathscr{V}|\cos\phi}{\sigma} e^{\frac{|\mathscr{V}|\cos\phi}{\sqrt{2}}}\left[1 + \mathrm{Ef}\left(\frac{|\mathscr{V}|\cos\phi}{\sqrt{2}\sigma}\right)\right]\right) \tag{A.21}$$

where Ef is the error function defined as:

$$\mathrm{Ef}\,(z) = \frac{2}{\sqrt{\pi}}\int_0^z e^{-t^2}\mathrm{d}t \tag{A.22}$$

$|\mathscr{V}|$ is the visibility vector (waveform at the correlator), $\mathbf{A} = Ae^{j\phi}$ is the signal plus noise vector. I_o is the modified Bessel function of zero order. The probability distributions are plotted in figure A.4 and figure A.5.

The standard deviation σ, is given by:

$$\sigma = \frac{\sqrt{2}kT_s}{A\eta_Q\sqrt{\Delta\nu_{IF}\tau_a}} \tag{A.23}$$

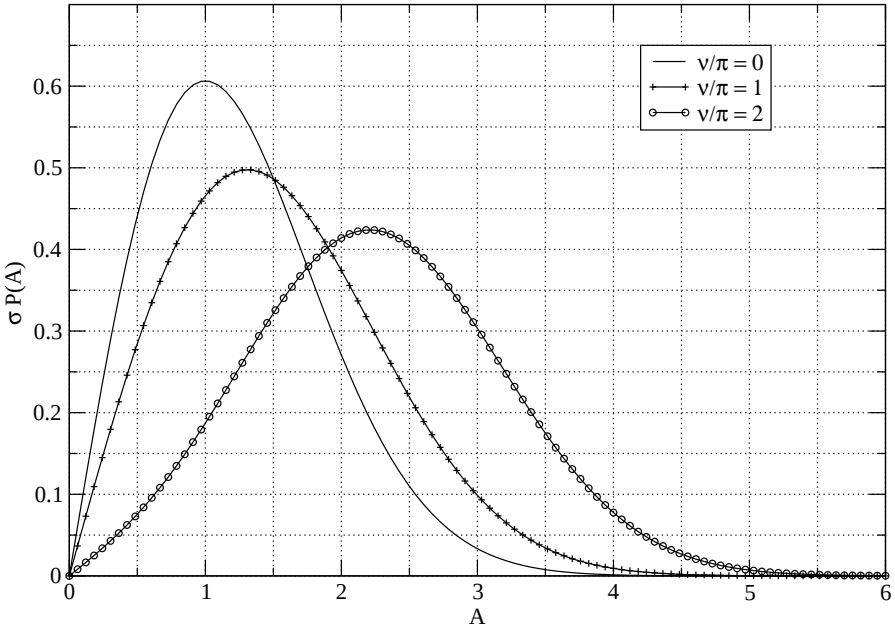


Figure A.5: Amplitude probability distributions

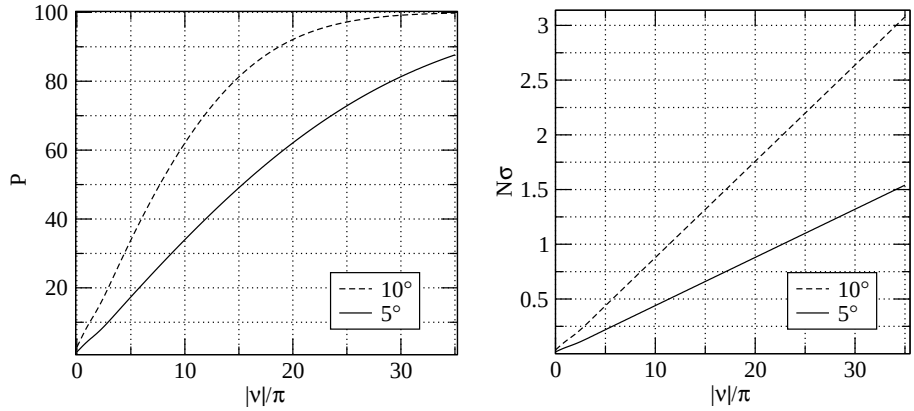


Figure A.6: Phase error probability

where $\Delta\nu_{IF}$ is the bandwidth, τ_a the integration time in seconds, A the antenna's surface area, η_Q represents the processing loss and T_s the system temperature.

The probability of a measurement lying within an error range of ε can be found as:

$$P_m = \int_{\phi-\frac{\varepsilon}{2}}^{\phi+\frac{\varepsilon}{2}} P(\phi)d\phi \tag{A.24}$$

with the associated confidence interval [15]:

$$N_\sigma = \sqrt{2}E_f(P_m) \tag{A.25}$$

The measurement probability and standard deviations of the correlations are calculated and plotted as figures A.6 and A.7.

The correlated SNR, with two antennas with system temperatures T_{s1}, T_{s2} and when pointed at a source giving antenna temperatures T_{a1}, T_{a2}, is:

$$\text{SNR} = \eta\sqrt{2\Delta\nu_{IF}\tau_a\frac{T_{a1}T_{a2}}{(T_{s1}+T_{a1})(T_{s2}+T_{a2})}} \tag{A.26}$$

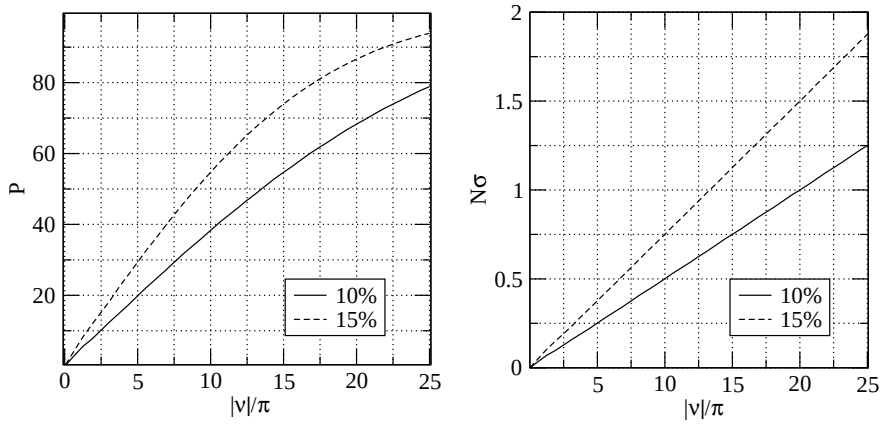


Figure A.7: Amplitude error probability

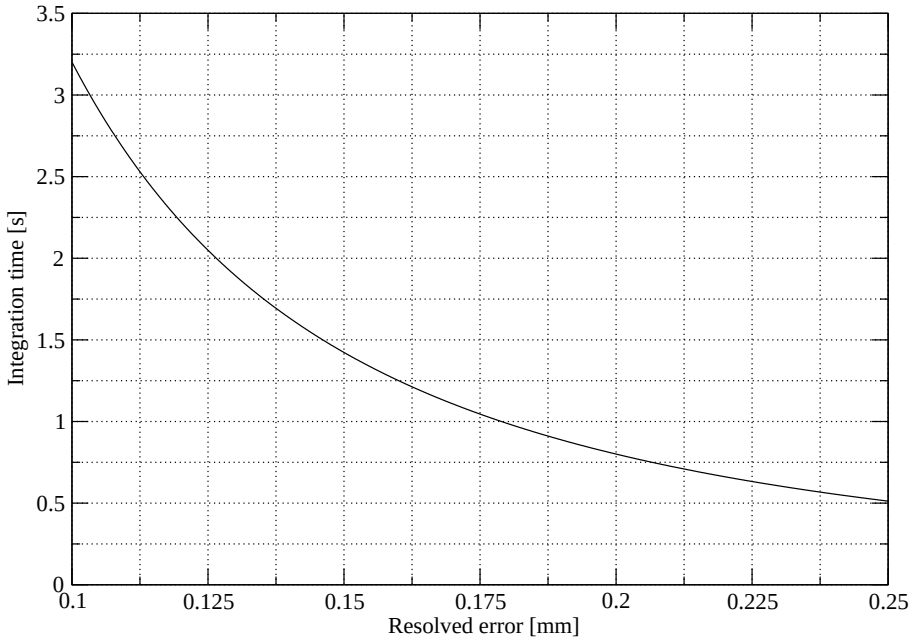


Figure A.8: Correlation time [s] vs resolvable surface error [mm] (N=64)

where $\eta \backsimeq 0.637$ represents the processing losses. This can be formally calculated as:

$$\eta = \eta_Q \eta_R \eta_S \eta_D \tag{A.27}$$

where:
$\eta_Q =$ quantisation loss (0.637 two-level)
$\eta_R =$ fringe rotation loss (0.9 one path)
$\eta_S =$ fringe sideband rejection loss (0.707 1 channel)
$\eta_D =$ Discrete delay step loss (0.966 video band centred correction)

Solving for $\eta = (.637)(0.9)(0.707)(0.966) = 0.39$. To solve for the required sample time equation A.26 is equated with equation A.18 and solved. Substituting in the system parameters and source parameters (calculated in [16] appendix C) the solution is plotted as figure A.8. From the graph each mapped point should be correlated for at least 3 s.

The correlation time of three seconds results in a minimium map times of: ≈ 0.85 hours for a $N = 32$ map, ≈ 3.41 hours for a $N = 64$ map and ≈ 13.65 hours for a $N = 128$ map.

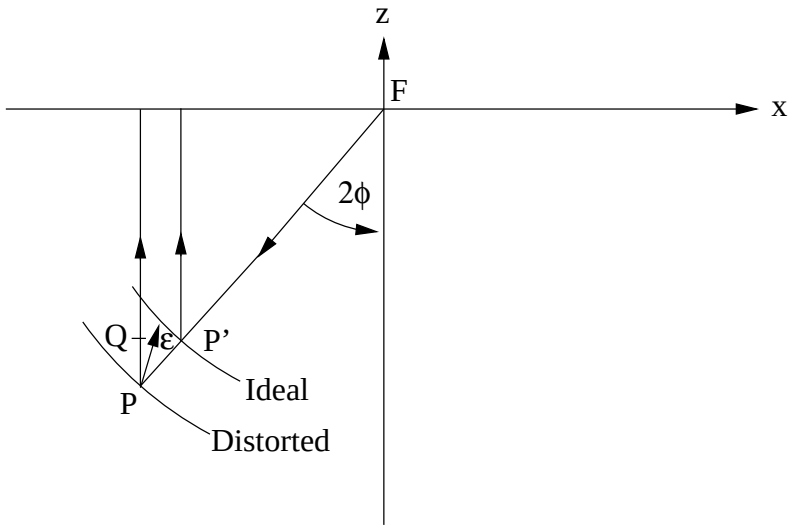


Figure A.9: Surface distortion geometry (adapted from [5])

A.5 Simulations

In order to test the theory and software reduction system, simulations of the map were required. The theory is based on the work done by *Rochblatt* [8].

A.5.1 Phase error

Surface errors are simulated using a geometric ray tracing model to construct a phase distribution. A surface displacement of ϵ creates an associated phase error due to a path length difference as shown in figure A.9. The error is calculated as follows [8]:

$$\begin{aligned}\frac{1}{2}\Delta PL &= \frac{1}{2}\left(P'P + PQ\right) \\ &= \frac{1}{2}\left(\frac{\varepsilon}{\cos\phi} + \frac{\varepsilon\cos 2\phi}{\cos\phi}\right) \\ &= \varepsilon\cos\phi\end{aligned} \tag{A.28}$$

The resulting phase error is:

$$\angle(\Delta PL) = \frac{4\pi}{\lambda}\varepsilon\cos\phi \tag{A.29}$$

substituting for a parabolic surface:

$$\cos\phi = \frac{1}{\sqrt{1+\frac{\rho^2}{4F^2}}} = \frac{1}{\sqrt{1+\frac{x^2+y^2}{4F^2}}} \tag{A.30}$$

rearranging equation A.29 and substituting equations A.5 and A.30 gives:

$$\varepsilon(x,y) = \frac{\lambda}{4\pi}\sqrt{1+\frac{x^2+y^2}{4F^2}}\angle(e^{j2kF}\mathscr{F}^{-1}[\mathbf{T}(u,v)]) \tag{A.31}$$

Equation A.31 relates surface errors to the measured beam pattern. i.e if **T** is known ε can be solved for. The simulation reverses the problem by specifying ε and calculates the phase of the beam pattern **T** which is then used for testing.

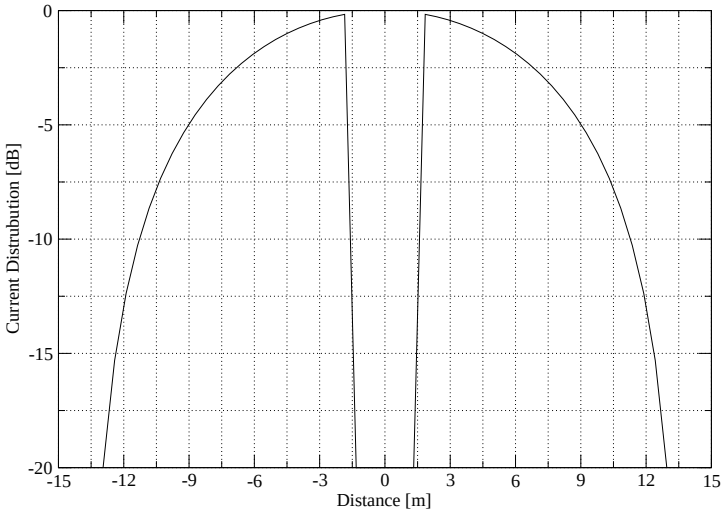


Figure A.10: Simulated current distribution across the HarRAO dish.

A.5.2 Current distribution

The current distribution is simulated as [6]:

$$J = B + C\left(1 - \rho^2\right)^2 \tag{A.32}$$

where:

$J =$ current distribution
$\rho =$ radial distance
$C =$ the roll off across the dish
$B = 1 - C$
edge taper $= 20 \log B$

Plotted as shown in figure A.10 and the associated simulated beam pattern in figure A.11 - the actual pattern is plotted for comparison (the main lobe is of primary interest, side-lobes discrepancies result from under-sampling). The taper is shaped by the sub-reflector and for HartRAO is 20 dB (typical for radio telescopes). The simulation is sufficient for the testing the software, for a more detailed discussion the reader is referred to *Potter* and *Rusch* [17].

In order to test the software a ring of panels is simulated as being displaced by 0.5 mm. The leg blockage is included, refer to [16] appendix B for the theory. The sampling theory presented in section A.3 is implicitly tested in the spacing of the simulated map. The reproduced surface is shown in figure A.12. The map is produced using the Australian Miriad software [18], using the Fourier algorithm and mapping software written by *Graves* and *Kesteven* [19].

A.6 Conclusions

The theory, broadly summarised, conformed to simulated results. The small angle assumptions made are negligible for large telescopes. The final estimated correlated times are reasonable and the method of cross-correlation is considered a good approach for holographic mapping. The requirements for source SNR and sampling accuracy are both usable for astronomical telescopes. The reduction software worked and returned the expected results. The mapping times, for larger maps ($N > 64$), would require careful scheduling within normal astronomical observing. Mapping should be separable so as to break it up and slot it between sources.

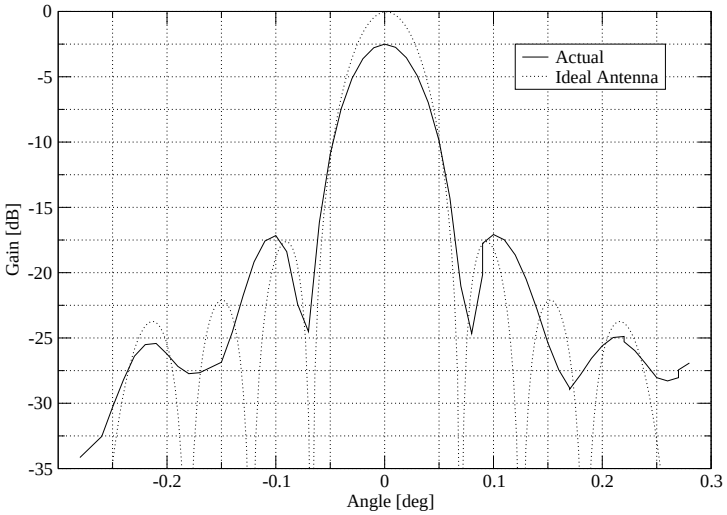


Figure A.11: Simulated beam pattern used to test holography imaging software (the actual beam is given for comparison).

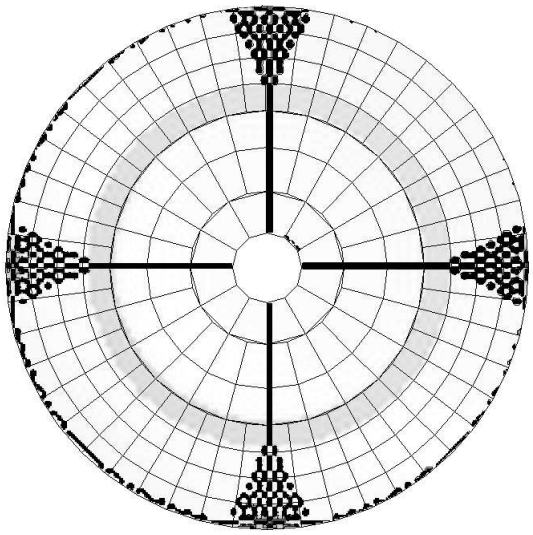


Figure A.12: Simulated holographic image produced from a generated beam pattern of a 26 m parabolic antenna with a ring of panels displaced by 0.5 mm, (blockage pattern is included).

References

[1] A. P. Anderson J. C. Bennett, Peter A. McInnes, and A. J. Whitaker. Microwave holographic metrology of large reflector antennas. *IEEE Transactions on Antennas and Propagation*, AP-24(3):295–303, May 1976.

[2] P. F. Scott and M. Ryle. A rapid method for measuring the figure of a radio telescope reflector. *Monthly Notices of the Radio Astronomy Society*, 178:539–545, August 1977. Mullard Radio Astronomy Observatory, Cavendish Laboratory, Madingley Road, Cambridge CB3 OHE.

[3] S. Silver. *Microwave Antenna Theory and Design*. McGraw-Hill Book Company, INC., 1949.

[4] John D. Kraus. *Antennas*. McGraw-Hill Book Company, INC., New York, Toronto, London, August 1950.

[5] Y. Rahmat-Samii. Surface diagnosis of large reflector antenna using microwave holographic metrology: An iterative approach. *Radio Science*, 19(5):1205–1217, September-October 1984.

[6] Yahya Rahmat-Samii. Microwave holography of large reflector antennas-simulation algorithms. *IEEE Transactions on Antennas and Propagation*, AP-33(11):1194–1203, November 1985.

[7] Y. Rahmat-Samii and V. Galindo-Israel. Shaped reflector antenna analysis using the jacobi-bessel series. *IEEE Transactions on Antennas and Propagation*, AP-28(4):425–435, July 1980.

[8] David J. Rochblatt. Microwave antenna holography. *IEEE Transactions on Microwave Theory and Technique*, 40(6):1294–1300, June 1992.

[9] Bryan Butler. Options for VLBA Antenna Surface Measurement. Technical report, National Radio Astronomy Observatory, March 1998. VLBA Test Memo. No. 57.

[10] Bryan Butler. Simulations of some types of holography errors for vlba antennas. Technical report, National Radio Astronomy Observatory, April 1999. VLBA Test Memo. No. 62.

[11] M. Kesteven, D. Grahamn, O. Lochner E. Fürst, and J. Neidhöfer. The Effelsburg Holography Campaign -2001. Max-Planck-Institut für Radioastronomie, October 2001.

[12] J. C. Bennett and M. P. Godwin. Necessary criteria for the diagnosis of panel misalignments in large reflector antennas by microwave meterology. *Electronic Letters*, 13:463–465, 1977.

[13] Kristen Rohlfs and Thomas L. Wilson. *Tools of Radio Astronomy*, volume 4. Springer-Verlag Heidelberg, New York, 2004.

[14] A. Richard Thomson, James M. Moran, and JR. George W. Swenson. *Interferometry and Synthesis in Radio Radio Astronomy*. John Wiley and Sons, New York, Chichester, Brisbane, Toronto and Singapore, 1986.

[15] Eric W Weisstein. Confidence interval. From MathWorld–A Wolfram Web Resource. http://mathworld.wolfram.com/ConfidenceInterval.html. Last visited June 2007.

[16] Benjamin Klein. Holographic measurement of the 26m hartrao telescope. Master's thesis, School of Electrical Enginnering, University of the Witwatersrand, Johannesburg, 2008.

[17] W. V. T. Rusch and P. D. Potter. *Analysis of Reflector Antennas*. Academic Press, Inc. (London) Ltd., Berkley Square House, London, WIX 6BA, 1970.

[18] Australian Telescope National Facility. Miriad. http://www.atnf.csiro.au/computing/software/miriad/. Last visited June 2007.

[19] G. Graves and M. Kesteven. Compact array holography. AT documentation, June 1995.

Appendix B

Holographic Physical System Considerations

B.1 Introduction

Holographic measurements require specifically tuned high frequency receiver systems [1]. In the case of two dish holography two systems need to be built and, as holography is a measurement of phase, synchronised to work together [2]. Astronomical microwave receivers are specialised radio frequency (RF) measurement systems, designed and optimised to receive specific low amplitude sources [3]. Consequently, measurement of astronomical telescopes requires adapting the astronomical system to receive satellite bands and levels. The reference system is built by adapting an existing satellite receiver system. The main telescope's K_u band (10.7 to 12.75 GHz) receiver system is presented along with the intermediate frequency (IF) system. The synchronisation of the mixing systems and associated local oscillators (LO) is given. Finally the calibration procedure and control and analysis software is discussed.

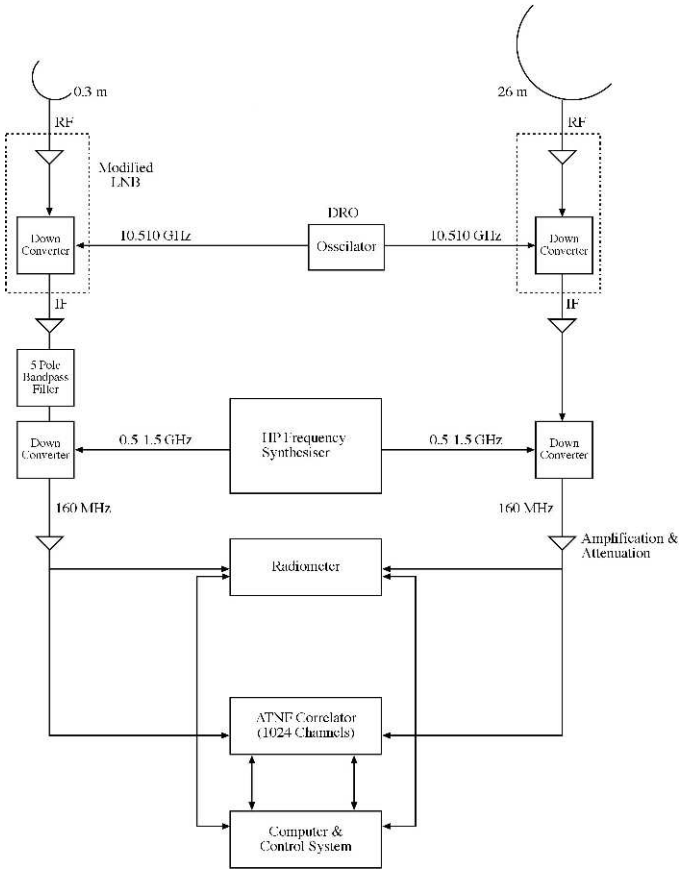


Figure B.1: System diagram.

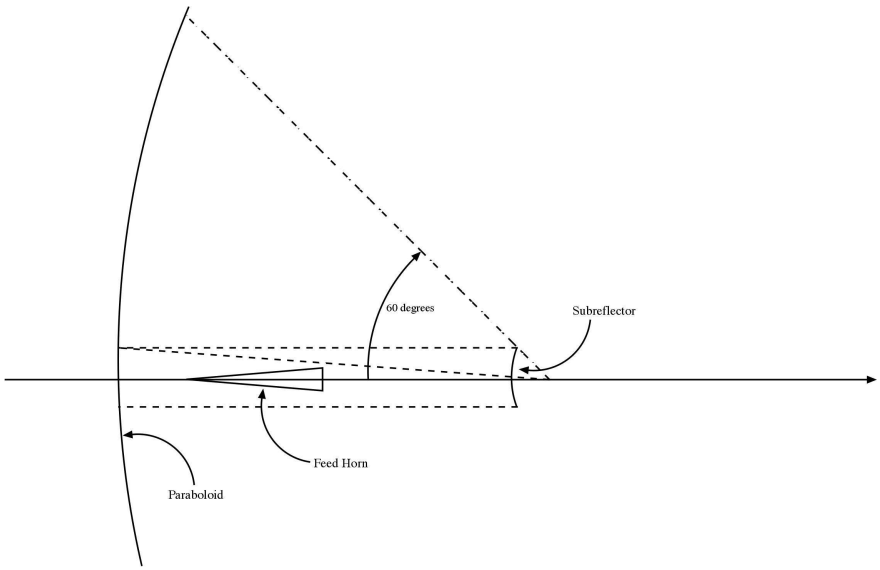


Figure B.2: Geometry of cassegrain antenna (adapted from [6]).

B.2 Receiver System

Radio astronomy is a specialised radio frequency application and normally economically expensive. The 12 GHz band (K_u band [4]), however, is utilised for satellite broadcasting. Consequently commercial hardware is available and a much cheaper system can be built by modifying off the shelf satellite low noise block converters (LNB)[1]. For holography, this has the added advantage as the system is configured for the required satellite source. The system gain, however, is tuned for low level astronomical sources and, in order to avoid saturation, filtering and attenuation is required. The reference antenna is also incorporated, while not interfering with daily astronomical monitoring. The overall system diagram is given in figure B.1, a two element interferometer consisting of the main 26 m dish and a reference dish. The signals are down converted to an IF of ≈ 1.5 GHz and then to the final 160 MHz at which it is measured and recorded. The main antenna is an astronomical research instrument, used both locally and internationally. It operates continuously and performs daily monitoring of radio sources. The system needed to be non-intrusive and be able to remotely switch in and out of routine observing. Electrical RF switching circuitry was used to switch in the required system components and out the astronomical receivers.

B.2.1 HartRAO Dish

The main telescope is a polar mounted cassegrain dish consisting of a feed illuminating a hyperbolic reflector which is in turn placed to reflect onto a parabolic reflector such that the transmit/received wave travels parallel to the surface. The configuration is shown in figure B.2. The beam pattern of the main reflector can be calculated using a ray tracing argument and Fourier transforming the resulting illumination function. The theory is discussed in [5] appendix A.

Feed

The feed is a dual-mode conical horn, (potter horn [7]), shown in Figure B.3. The horn is defined as follows [8]:

[1]Limited to ambient systems

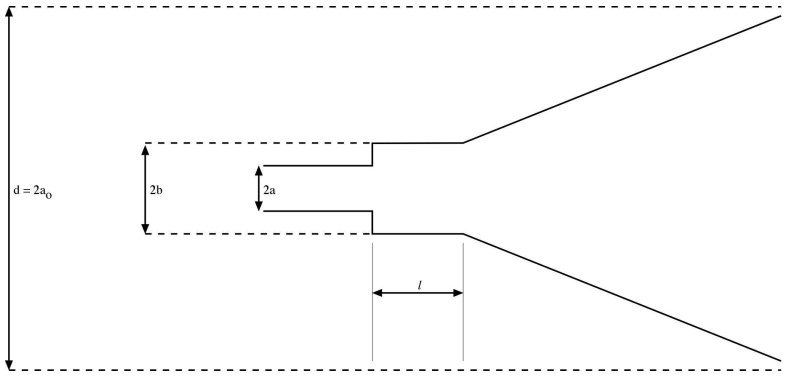


Figure B.3: Dual-mode potter horn.

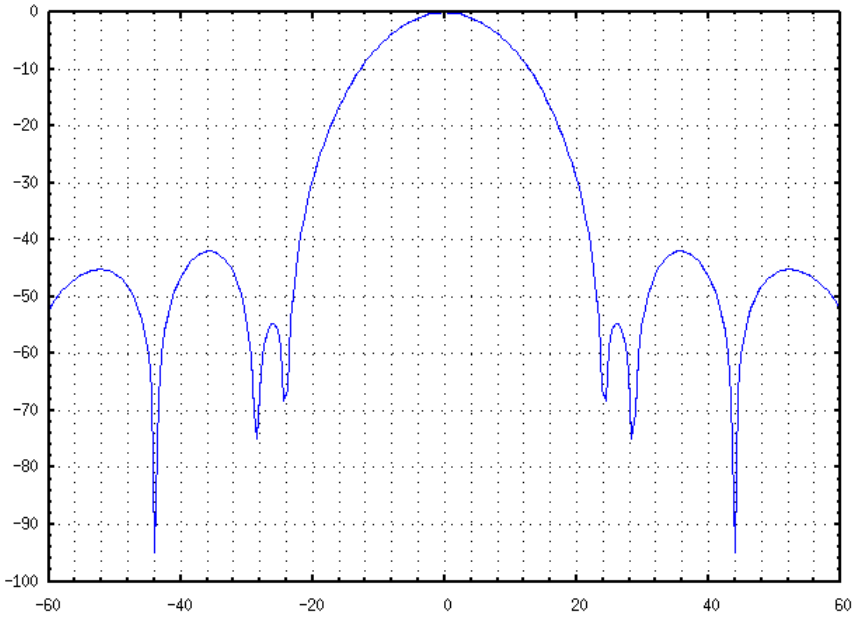


Figure B.4: Dual-mode horn beam-pattern amplitude [dB] vs. angle [deg].

$$
\begin{aligned}
E_\theta &= \left[1 + \frac{\lambda}{\lambda_g}\cos\theta - \alpha\frac{\lambda/\lambda_g' + \cos\theta}{1-(3.83/u)^2}\right]\frac{J_1(u)}{u}\cos\phi \\
E_\phi &= \left(\frac{\lambda}{\lambda_g} + \cos\theta\right)\frac{J_1'(u)}{1-(u/1.84)^2}\sin\phi
\end{aligned}
\tag{B.1}
$$

Where $u = 2.34\,\lambda\,\mathrm{k}\sin\theta$, $(1.84 < ka < 3.83)$, $(3,83 < kb < 5.33)$, $\lambda/\lambda_g = 1$, $\lambda/\lambda_g' = 0.96$, $\alpha = 0.6$, J_1 is a first order Bessel function and J_1' is its differential [8]. The receiver is optimised to suppress side lobe levels and reduce ground noise. This design gives a HPBW $\approx 14.5^\circ$ resulting in a 20dB edge taper across the hyperbolic reflector and consequently 20dB taper at the edge of the main parabolic reflector. The beam pattern is shown in figure B.4.

Hyperbolic reflector

The hyperbolic reflector is a 3 m dish mounted at the primary focus, such that its focus is coincidental with the main parabolic dish's focus. The hyperbolic reflector is flanged slightly to reduce ground interference as shown in figure B.5, for a detailed discussion refer to work by *Rusch* [9]. Based on this work the scattered pattern can be derived as shown in [5] appendix D. The result, practically is computational expensive and a ray tracing approximation is sufficient (the observing frequency is high and the dish electrically large).

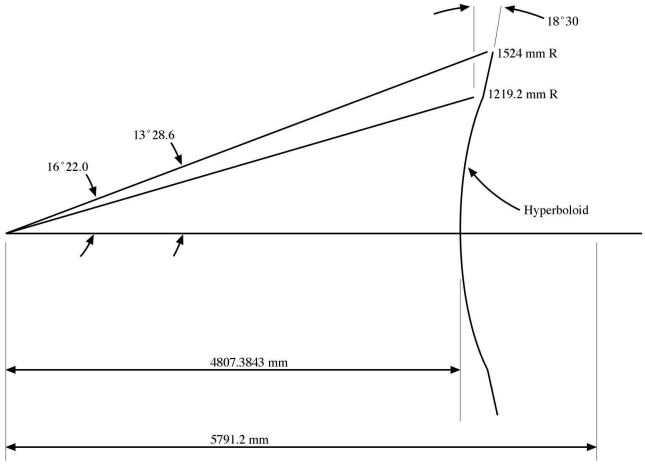


Figure B.5: Hyperbolic reflector geometry, showing flanges (adapted from *Bathker* [10]).

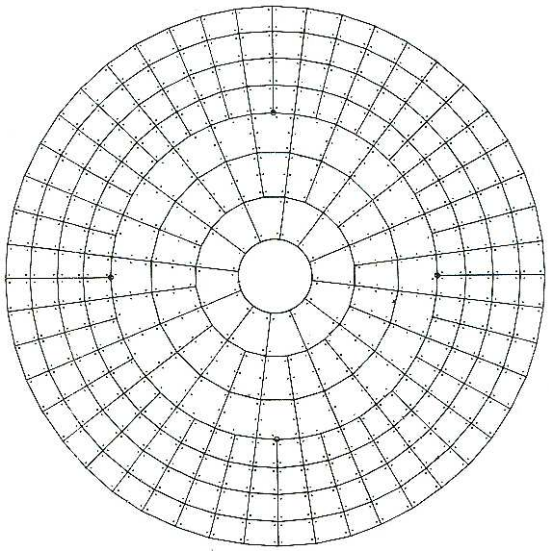


Figure B.6: Panel map of parabolic reflector, shown with associated adjustment screws.

Parabolic reflector

The surface consists of 252 solid panels configured as shown in figure B.6. Each panel has at its edges adjustment screws allowing it to be moved freely (without distortion) in three dimensions. Adjustment of the surface are limited to moving the panels.

Leg Blockage

The HartRAO dish consists of four leg supports for the hyperbolic reflector which partially obscure the main reflector. The leg's shadow up to where the leg reaches the surface is a linear blockage with the width of the leg. Beyond where the support legs attaches to the surface the blockage is a 'spherical wave' shadow described as [11]:

$$A_{bs} = \frac{W_l}{AB}\left(\frac{R_p^2 - R_q^2}{2} - (R_p - R_q) f \tan\alpha + \frac{\tan\alpha}{12f}(R_p^3 - R_q^3)\right) \tag{B.2}$$

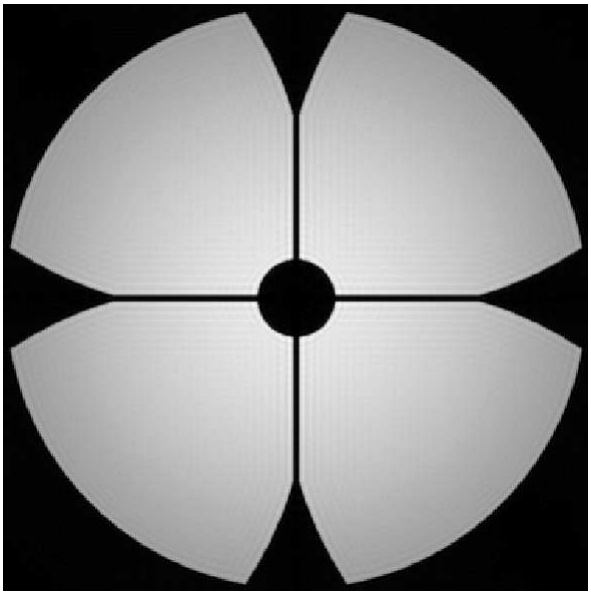


Figure B.7: Plots of simulated support structure blockage.

where:

$$
\begin{aligned}
AB &= R_q(1 - \tan\alpha/\tan\psi) \\
\psi &= 2\arctan\frac{R_q}{2f} \\
R_p &- \text{radius of the parabolic reflector (projected)} \\
R_q &- \text{radius of the hyperbolic reflector (projected)} \\
f &- \text{parabolic focal length} \\
W_l &- \text{width of leg} \\
\alpha &- \text{angle with respect to main antenna axis}
\end{aligned}
$$

Equation B.2 is for a uniform illumination pattern, for a -11 db taper at the edge the correcting term to be subtracted is:

$$A_{bsc} = \frac{0.7W_l}{ABR_p^2}\left(\frac{R_p^4 - R_q^4}{4} - f\tan\alpha\frac{R_p^3 - R_q^3}{3} + \frac{\tan\alpha}{20f}(R_p^5 - R_q^5)\right) \tag{B.3}$$

The computed results are plotted in figure B.7 (the central blockage is that of the sub-reflector).

B.2.2 Reference Dish

For simplicity, the reference dish is sized in order to avoid tracking the satellite. The dish is either mounted near the dish in a fixed location or on the main dish. In the former case the beam must be greater than the satellite movement. Geostationary satellites move by less than a degree (refer to [5] appendix C) and thus a HPBP of 2° is a minimum to allow for a setting accuracy of 0.5°. In the latter case the limiting factor is the movement of the main telescope. For the required holographic map of 64 points this requires a beam-width of 4°, to allow for setting error of 0.5° puts the beam at 5°. Calculating the half power beam width (HPBW), using HPBW $= 1.2\lambda/\mathrm{D}$ [12], the reference dish size is calculated as a maximum of 2 m and 0.45 m respectively.

If the dish is mounted on the main dish, it is aligned to the the main dish and pointing is handled by the telescope drive systems allowing easy configuration and switching between satellites.

Mounting the dish separately, it is pointed at the satellite and fixed. All the satellites to be considered are geostationary and consequently found on the equatorial arc. For polar mounted dishes it is possible to set the declination of the dish in order to approximately drive along this arc in the hour angle direction. This eases the location and possible switching of satellites. The solution for HartRAO's location are given in [5] appendix E.

B.2.3 IF components

The HartRAO telescopes is configured to observe multiple frequency bands which are alternatively switched in. The system, as a result, has two stages of down conversion; the first from the 12 GHz RF to 1.5 GHz in order to range it within the general system and then to a standard 160 MHz, used in the measurement and analysis system. This requires two mixer stages and thus two oscillators.

B.2.3.0.1 Mixers: The first mixer stage is a standard satellite block converter modified to bypass the built in oscillator (the original oscillator cannot be phase locked and is unusable). The oscillator circuitry is disabled and hard line is used to inject the required signal into the mixer circuitry. The secondary mixer is a high quality, low noise image rejection (single side band) mixer with 25 dB rejection and negligible phase noise [13].

B.2.3.0.2 Bandpass Filter: Geostationary satellites are, typically, used to transmit to fixed ground receivers (eg. digital satellite TV receivers). Consequently they contain high power broadband carriers. In principle this can be considered random noise and used for holography, however this overpowers the receiver. Along with the broadband communication a low power narrow band beacon signal is transmitted for locking, this is preferentially used. In order to prevent saturation the bandpass signal is filtered out. The filter is based on the design by *Hinshaw* and *Monemzadeh* [14]. It is possible to build a narrower filter, however the digital filter available requires a high level of random noise in order to operate linearly.

B.2.3.0.3 Digital Filter: The digital filtering mechanisms designed for astronomical correlators operate under an assumption of high noise ratios (as is the case in radio astronomy). The filter's behaviour in the case of strong a continuous wave (CW) signal is not well defined. In order to avoid this a large bandwidth is used to bring the filter into an operational range, 4 MHz is used. The bandwidth used must, for calibration, match the bandwidth of the radiometer.

B.3 Oscillator distribution

Two oscillators are required per receiver chain to down convert the RF to 160 MHz. Noise on the oscillator is linearly summed into the noise of the RF signal [2] and is critical to the measurement.

B.3.1 Phase Noise

The measured phase noise in the system using a single phase lock loop (PLL) is plotted in figure B.8. The noise is too high for Holography ($\sigma \approx 16^\circ$). Measurement of the individual sections of the system shows that the noise is associated with the PLL. The locking oscillator is a 5 MHz atomic Maser with (for this case) near perfect phase. Long cable length ($\approx$ 200m) used in distributing the locking system however add noise. The high frequency oscillator (10.510 GHz), used in the first down conversion, is shared between both system in order to defeat the noise associated with the single PLL loop system. This adds the complexity of requiring a high frequency distribution system.

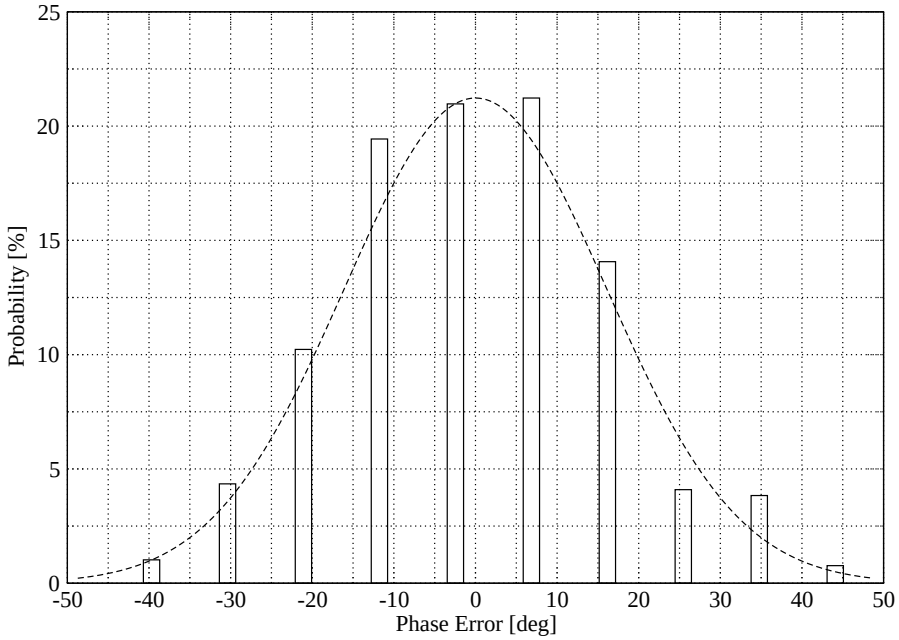


Figure B.8: Histogram of measured phase noise on a single PLL at 10.510 GHz, $\sigma = 16^{\circ}$.

B.3.2 Phase Stabilisation

B.3.2.0.4 High Frequency Transmission: Circular waveguide is a good low loss stable transmission option (high quality phase stable cables with low loss, although available, are economically expensive). The attenuation factor, α, for circular waveguide can be calculated as follows [15]:

$$\alpha = \frac{0.18623}{a^{3/2}} \sqrt{\frac{R_{\text{Cu}}}{R_{\text{Al}}[(f/f_c)^3 - (f/f_c)]}} \tag{B.4}$$

Where a is the radius of the pipe, f is the frequency f_c is the cut off frequency given as $c/1.640a$ for the $TE_{0,1}$ mode and R is resistivity. Using standard pipe size, the lock oscillator can be transmitted at a loss of 0.04 dB/m at 10.510 GHz. For tens of meters the major loss factor is the waveguide/cable transmission which have measured loss of 1.5 dB/transmission. Standard pipe sizes are used for the advantage of cost and allow easy fitting of temperature stabilising sheathing. Alternatively low loss cable is available (however expensive).

B.3.2.0.5 PLL schemes: Several options are available to stabilise the LO system used to lock the high frequency oscillators. The reader is referred to *Legg* [16] and *Little* [17], for solutions.

B.4 Phase variation

Attaching the feed to the antenna structure introduces a phase variation resulting from differential movement of the phase centres of the antennas. This is calculated and corrected for. The phase variation is a result of the changing distance between the two feeds and the satellite source. The geometry of the antenna and reference dish is given in figure B.9, the rotational axes of the main antenna and associated angles θ, ϕ are shown. The height differential between the antenna phase centres is the dot product between the differential vector and the pointing vector to the satellite $\mathbf{z} \cdot \mathbf{D}$. The vector $\mathbf{D}$ rotates with the telescope as it changes its pointing. The vector is modified using the rotational matrices R_x, R_y [18]. The solution is given below:

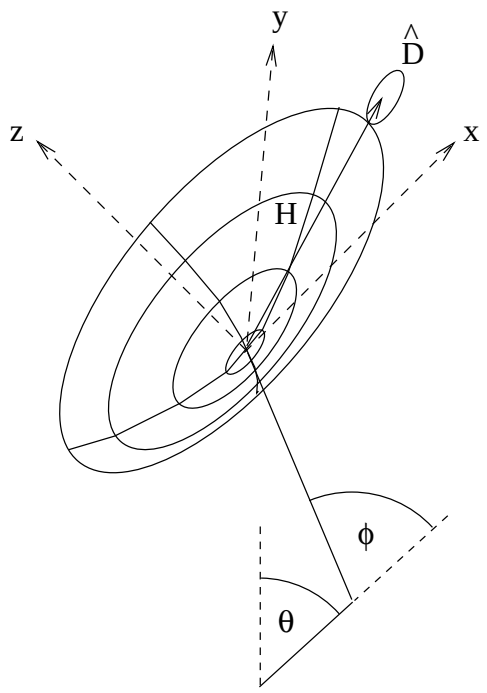


Figure B.9: Main antenna geometry with attached reference dish.

$$
\begin{aligned}
H =& \mathbf{z} \cdot R_x R_y \begin{pmatrix} D_x \\ D_y \\ D_z \end{pmatrix} = \mathbf{z} \cdot \begin{pmatrix} 1 & 0 & 0 \\ 0 & \cos\phi & \sin\phi \\ 0 & \sin\phi & \cos\phi \end{pmatrix} \times \\
& \begin{pmatrix} \cos\theta & 0 & -\sin\theta \\ 0 & 1 & 0 \\ \sin\theta & 0 & \cos\theta \end{pmatrix} \begin{pmatrix} D_x \\ D_y \\ D_z \end{pmatrix} \\
=& D_y \sin\phi + D_z \cos\theta \cos\phi
\end{aligned}
\tag{B.5}
$$

The variation in phase to be correct for is the difference between the phase calculated on the bore-site (bs) to each recorded point (n).

$$
\angle_{\triangle} = 2\pi \frac{H_{\text{bs}} - H_{\text{n}}}{\lambda} \tag{B.6}
$$

The reference antenna is sized to minimise its affect on the measurement however the measurement range will add a small effect from its beam shaped. The effect is accumulative in the measurement and cannot be directly measured and consequently has to be calculated and removed numerically. An offset reflector is the most readily available of dish for K_u band systems. The field equations, are derived by *Maclean* [19]. For the used dish of 0.3 m it is considered negligible for the produced maps, however if larger maps of $N = 128$ are required it would need to be calculated and removed.

B.5 Calibration

The measurement is referenced to the central point of the map (the bore-site), as the length of the measurement can be significant, in order to resolve out drifts this point needs to be re-measured periodically (every few hours). Unlike astronomical measurements however, holography does not need to resolve absolute amplitudes but relative amplitudes.

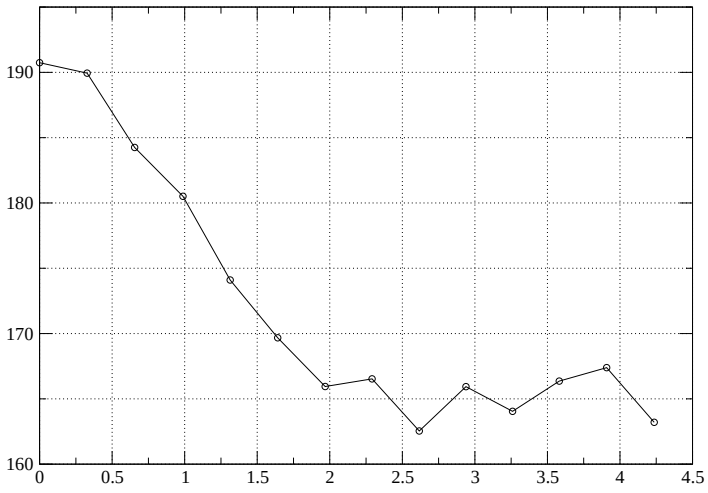


Figure B.10: Bore-site phase data.

B.5.1 Amplitude

The astronomical receiver is calibrated using a variation on the standard noise diode method [20]. Typically, in radio astronomy, the receiver level is measured by turning on a noise diode and injecting its signal into the waveguide as close to the feed as possible. To obtain the systems zero level a standard $50\ \Omega$ load is used at the input to the detector. The measured amplitude is zeroed and scaled by the know value of the diode. In the holographic system, the reference dish has no noise diode and instead its auto-correlation is measured and used to track gain variations in the system. A radiometer is used to measure the total power of both channels and track system temperature changes. The cross correlation is scaled using automatic gain control (AGC) and recorded as a raw, dimensionless quantity. The data is calibrated to a meaningful value by scaling it by the system temperature to convert it to Kelvins. The system temperature is the ratio between the total power recorded TP (in Hz) and the noised diode calibrator recorded H in Hz$/K$. The calibrated auto-correlation A is given in equation B.7 and the calibrated cross-correlation C in equation B.8.

$$A = A_{\text{meas}} \frac{TP_{\text{R}}}{H_{\text{R}}} \tag{B.7}$$

$$C = C_{\text{meas}} \sqrt{\frac{TP_{\text{M}} TP_{\text{R}}}{H_{\text{M}} H_{\text{R}}}} \tag{B.8}$$

Where, A_{meas} and C_{meas} are the measured values directly from the correlator and the M and R subscripts indicate the main and reference system respectively. In order to obtain a measured power of the antenna's gain M_{gain}, independent of variations in the satellite strength and reference antenna gain, the calibrated cross-correlation C must be divided by the square root of the auto-correlation A, as follows (shown in equation B.9):

$$\begin{aligned} M_{\text{gain}} &= C_{\text{meas}} \sqrt{\frac{TP_{\text{M}} TP_{\text{R}}}{H_{\text{M}} H_{\text{R}}}} \times \sqrt{\frac{H_{\text{R}}}{A_{\text{meas}} TP_{\text{R}}}} \\ M_{\text{gain}} &= C_{\text{meas}} \sqrt{\frac{TP_{\text{M}}}{A_{\text{meas}} H_{\text{M}}}} \end{aligned} \tag{B.9}$$

The M_{gain} is in volts. The final gain is independent of the reference dish's system temperature as expected.

B.5.2 Phase

Phase calibration is done periodically on the bore-site, variations during the measurements are modelled out. Phase drift must consequently be close to linear during the measurement and lower than a 180° rate in order

to resolve out phase wrapping. The measured system phase drift over several hours is plotted in figure B.10 - as the bore-site is measured a few times every hour the variation is sufficiently slow and linear to remove.

B.6 Software

The data is recorded into the standard format FITS [21] and later reduced using custom routines written using the mathematical package Octave [22]. The Fourier transform is calculated and the images are produced using the astronomical image processing system (AIPS) [23] and Miriad packages [24]. The specific routine is detailed by *Graves* and *Kesteven* [25].

B.7 Conclusions

The modifications of the astronomical receiver worked correctly and enable the main receiver to operate within the required satellite band and higher signal levels. The modified satellite system (to be used as the reference system) also worked correctly. The overall system does not impact normal observing. Phase variations between the system is considered sufficiently low and the modifications, to synchronise the systems, worked correctly. Calibration and software reduction worked well and performed as expected. Overall, the system is considered sufficient to perform the holographic measurement.

References

[1] P. F. Scott and M. Ryle. A rapid method for measuring the figure of a radio telescope reflector. *Monthly Notices of the Radio Astronomy Society*, 178:539–545, August 1977. Mullard Radio Astronomy Observatory, Cavendish Laboratory, Madingley Road, Cambridge CB3 OHE.

[2] A. Richard Thomson, James M. Moran, and JR. George W. Swenson. *Interferometry and Synthesis in Radio Radio Astronomy*. John Wiley and Sons, New York, Chichester, Brisbane, Toronto and Singapore, 1986.

[3] Kristen Rohlfs and Thomas L. Wilson. *Tools of Radio Astronomy*, volume 4. Springer-Verlag Heidelberg, New York, 2004.

[4] IEEE Standard 521-2002. Standard letter designations for radar-frequency bands, 2003.

[5] Benjamin Klein. Holographic measurement of the 26m hartrao telescope. Master's thesis, School of Electrical Enginnering, University of the Witwatersrand, Johannesburg, 2008.

[6] W. V. T. Rusch. Phase error and associated cross-polarization effects in cassegrainian-fed microwave antennas. Technical Report 32-610, Jet Propulsion Laboratory, May 1964.

[7] W. V. T. Rusch and P. D. Potter. *Analysis of Reflector Antennas*. Academic Press, Inc. (London) Ltd., Berkley Square House, London, WIX 6BA, 1970.

[8] Richard C. Johnson and Henry Jasik, editors. *Antenna Engineering Handbook*. McGraw-Hill Book Company, INC., second edition, 1984.

[9] W. V. T. Rusch. Scattering from a hyperboloidal reflector. Technical Report 32-283, Jet Propulsion Laboratory, July 1962.

[10] Dan A. Bathker. Radio-frequency performance of an 85-ft ground antenna: X-band. Technical Report 32-1300, Jet Propulsion Laboratory, July 1968.

[11] Jacob W. M. Baars. Characteristics of a reflector antenna. Technical report, ESO/ NRAO, Tucson AZ, April 2003. ALMA Memo 456.

[12] John D. Kraus. *Antennas*. McGraw-Hill Book Company, INC., New York, Toronto, London, August 1950.

[13] Miteq. *Image rejection products*, 2003.

[14] Jerry Hinshaw and Shahrok Monemzadeh. Computer-aided interdigital bandpass filter design. *Ham radio magazine*, pages 12–26, January 1985.

[15] H. P. Westman, editor. *Reference data for radio engineers*, chapter 23. Howard W. Sams and CO., 1974.

[16] T. H. Legg. Microwave phase comparators for large antenna arrays. *IEEE Transactions on Antennas and Propagation*, 1964.

[17] Alec G. Little. A phase-measuring scheme for a large radiotelescope. *IEEE Transactions on Antennas and Propagation*, Ap-17(5), September 1969.

[18] Eric W Weisstein. Rotation matrix. From MathWorld–A Wolfram Web Resource. http://mathworld.wolfram.com/RotationMatrix.html. Last visited June 2007.

[19] T. S. M. Maclean. *Principles of antennas: wire and apeture*. Cambridge University Press, 1986.

[20] M. Kesteven, D. Grahamn, O. Lochner E. Fürst, and J. Neidhöfer. The Effelsburg Holography Campaign -2001. Max-Planck-Institut für Radioastronomie, October 2001.

[21] Fits the astronomical image and table format. http://fits.gsfc.nasa.gov/. Last visited June 2007.

[22] Gnu octave. http://www.gnu.org/software/octave/. Last visited June 2007.

[23] NRAO. Astronomical image processing system. http://www.aips.nrao.edu/. Last visited June 2007.

[24] Australian Telescope National Facility. Miriad. http://www.atnf.csiro.au/computing/software/miriad/. Last visited June 2007.

[25] G. Graves and M. Kesteven. Compact array holography. AT documentation, June 1995.

Appendix C

Satellite Considerations

C.1 Introduction

Microwave holographic measurements, ideally, require a high power, stable and still source [1], [2]. Geostationary satellite beacons are well suited, satisfying all the requirements. The following document considers numerous satellite choices and discriminates between them based on critical and desirable characteristics. The satellite requires tracking and as it cannot be directly measured during the measurement, its movement must be predictable. Its motion is modeled and the prediction is compared against measured positions. The available signal is calculated and conclusions are stated.

C.2 Satellite Choices

Being geostationary, for each satellite only one antenna position can be measured and thus as many satellite options should be considered so as to allow for the possibility of multiple measurements to map out gravitational distortions.

C.2.1 Requirements

In order for a satellite to be usable it must have the following properties:

- Visible at the Hartebeesthoek radio observatory (HartRAO) (10° to 66° East)
- Have a frequency in the receiver band (11.5 to 12.5 GHz)
- The beacon must have a footprint with sufficient power over Gauteng
- The ephemeris data must be updated regularly.

Additionally, for discriminating between satellites the following properties are desirable, ranked from most to least.

1) As close to the zenith position of the antenna so as to average out gravitational distortions.
2) The broadband carrier must not swamp the receiver and saturate the amplifiers. Preferably the beacon should be outside the carrier to allow filtering.
3) Stable beacon frequency
4) Operational lifetime of several years.

C.2.2 Satellite Option

To locate available satellites a media search and a power scan on the sky was done. The found, usable satellites are given in table C.1.

Table C.1: Satellite options arranged according to Hour Angle.

Satellite Name	Longitude East	Hour Angle [deg]	Beacon Frequency [GHz]	Beacon Power [dBW][1]
Bonum 1	56	32.51	11.706	-
Europe Star 1	45	19.98	11.697	-
Eurasiasat 1	42	16.53	11.699	-
Eutelsat Sesat	36	9.62	11.450	9
Eutelsat W4	36	9.62	11.706	9
Eurobird	28.2	0.6	11.200	-
Astra 1B	19.2	-9.81	11.6965	16
Eutelsat W2	16	-13.51	11.6992	9
Hot Bird 5	13	-16.96	11.6998	8
Eutelsat W1	10	-20.4	11.451	9
Eutelsat W3	7	-23.84	12.501	9
Sirius 2	5	-26.11	11.7768	-

1 unpublished data would need to be measured, typically the minimum beacon power is 4 dBW.

The satellite decided upon was Eutelsat W2. Eutelsat w2 has a beacon which sits in a narrow 10 MHz band free of the satellite's broadcast spectrum - allowing for ease in filtering. Additionally it has the required power, ephemeris stability and position in the sky.

C.3 Technical considerations

The primary concerns for the holographic measurement are those of phase.

C.3.1 Tracking

Geostationary satellites although highly stable, drift appreciable within the beam of the telescope (HPBW $\approx 0.059^\circ$ at 12 GHz) and consequently are actively tracked periodically throughout the measurement. Stable geostationary satellites trace out a elliptical orbit that is defined using the classical Kepler model defined as [6]:

$$\theta = 2\,\text{ecc} \times \sin(k(t - t_0) - w) - .25\,\text{inc}^2 \times \sin(2k(t - t_0)) \tag{C.1}$$

$$\phi = \text{inc} \times \sin(k(t - t_0)) \tag{C.2}$$

Where:

$k = \tan^2(ha) + \tan^2(dec)(1 + \tan^2(ha))$
inc - satellite inclination
ecc - satellite eccentricity
$t_0 -$ satellite epoch(time when satellite,
moving north, crosses the equatorial plane)
$t -$ time since epoch
$w -$ argument of perigee

The orbit, for a geostationary satellite (with parameters modeled on Eutelsat W2), is plotted in figure C.1.

The Kepler model is an ideal case and does not account for systematic drifts and variations. In order to cope with this the maintainers of the satellite provide an updated ephemeris model periodically. The standard

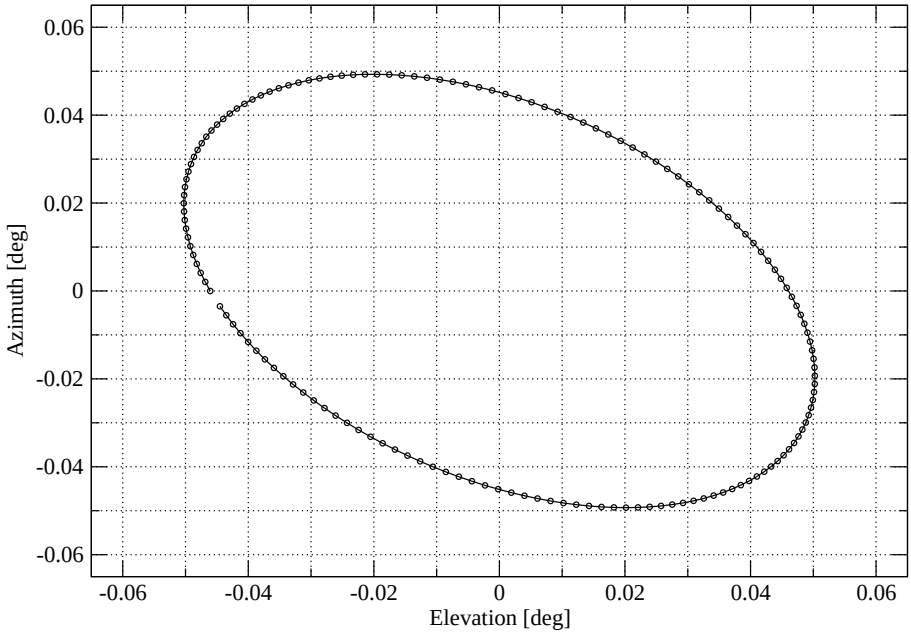


Figure C.1: Predicted movement of geostationary satellite in the az, el plane, over 24 hours using a Kepler model.

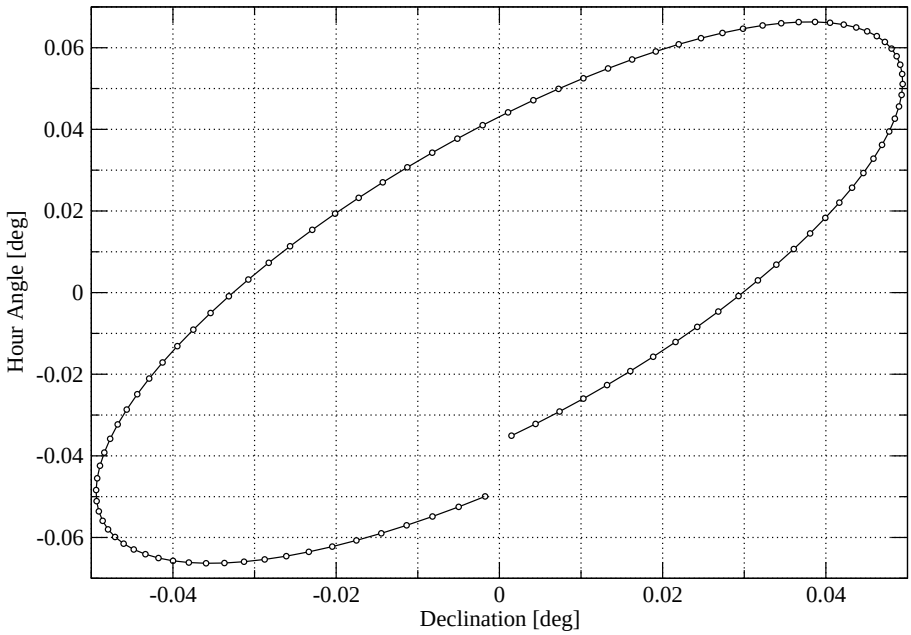


Figure C.2: Predicted movement of satellite Eutelsat W2 in the observed dec, ha plane, over 24 hours using the NORAD model.

model used is the NASA/NORAD Two-Line Element Set format provided by CelesTrak[4]. The prediction is plotted in figure C.2. The predicted drift for Eutelsat W2 is $\approx 0.1^\circ$.

The accuracy of the prediction is determined by the modeled parameters accuracy and the age of the ephemeris. CelesTrak does not return the accuracy of the prediction directly however it possibly to estimate the deviation of the prediction over time using the model itself [5]. By comparing an older ephemeris with a more recent one the stability or the speed at which the model degrades is measured. Simulations show that over the modeled period, approximately three days for Eutelsat W2, this varied by $\approx 0.03^\circ$.

Offsets in the model are found periodically during the map (every few hours) by performing a series of

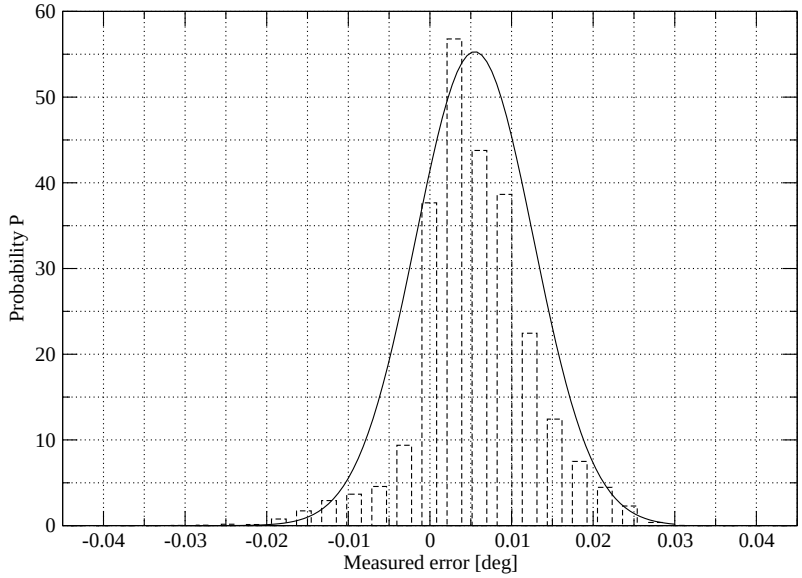


Figure C.3: Probability distribution P P $(\overline{P}, P_\sigma) = (5.48, 7.21)$ m° of the error in NASA/NORAD geostationary satellite model in the dec plane, measured using a series of cross scans.

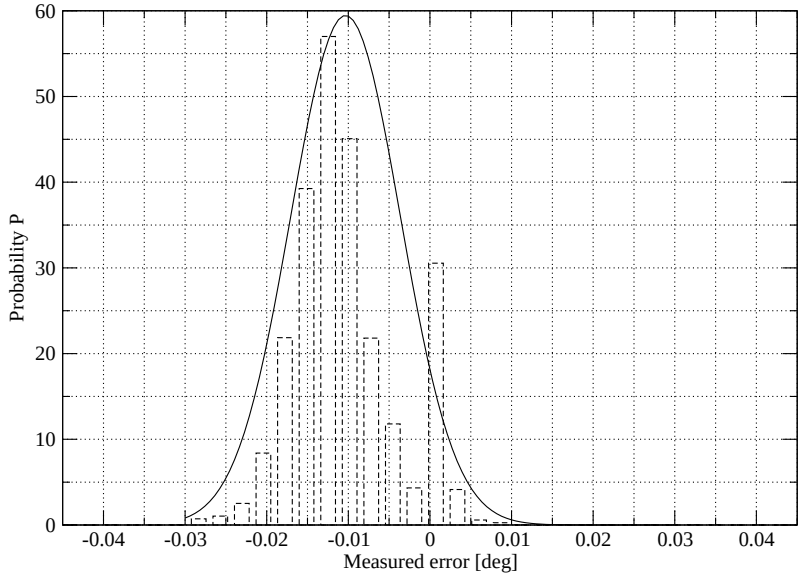


Figure C.4: Probability distribution P $(\overline{P}, P_\sigma) = (-10.34, 6.71)$ m° of the error in NASA/NORAD geostationary satellite model in the ha plane, measured using a series of cross scans.

iterative cross scans to centre on the satellite and find the offset from the prediction. The statistical error directly measured (for Eutelsat W2) are plotted as figure C.3 and C.4. The error has a systematic error due to offsets in the antenna's pointing model. This error is removed with an initial cross scan before the map is started.

C.3.2 Received power

The received power per Hz from the beacon signal is [3]:

$$P = \eta \times \text{Flux} \times \text{Area} = \eta \frac{\text{EIRP}}{4\pi R_S^2} \pi R_D^2 = \frac{\eta}{4} \text{EIRP} \left(\frac{R_D}{R_S} \right)^2 \tag{C.3}$$

Where R_S is the distance to the satellite (≈ 36000 km), R_D is the diameter of the dish (0.3 m), η is the efficiency of the antenna ($\approx 50\%$) and EIRP is the effective isotropic radiated power of the beacon signal. The noise power spectral density (N_{PSD}) given an antenna temperature T and a correlator channel bandwidth B is calculated using Boltzmann law.

$$N_{\text{PSD}} = kTB \tag{C.4}$$

For the chosen satellite Eutelsat w2 the beacon power above the noise is 30 dBm, for the given correlator channel bandwidth. The resulting antenna temperature looking at the source T_a is:

$$T_a = \frac{\text{AS}}{2k} \tag{C.5}$$

Where S is the flux density on the source given by:

$$\text{S} = \frac{\text{EIRP}}{\Delta\nu_{IF}\, 4\pi R_S^2} \tag{C.6}$$

Where $\Delta\nu_{IF}$ is the correlator bandwidth. Solving Equation C.5 gives a temperature on source of $T_s \approx 300$ K. The consequences for holography measurement is discussed in detail in appendix A.

C.4 Conclusions

The use of a geostationary satellite, to perform the holographic measurement, is possible from HartRAO. Several options are present with the correct elevation and sufficient power and stability to meet the requirements. The satellite to be used is Eutelsat W2.

References

[1] Bryan Butler. Options for VLBA Antenna Surface Measurement. Technical report, National Radio Astronomy Observatory, March 1998. VLBA Test Memo. No. 57.

[2] Rochblatt David J and Yahya Rahmat-Samii. Effects of measurement errors on microwave antenna holography. *IEEE Transactions on Antennas and Propagation*, 39(7):933–942, July 1991. 1991.

[3] G. Graves and M. Kesteven. Holography instrumentation. Technical report, ATNF, May 1999.

[4] Dr. T.S. Kelso. Celestrak. http://celestrak.com/. Last visited June 2007.

[5] Dr. T.S. Kelso. More frequently asked questions. Satellite Times online at http://celestrak.com/columns/v04n05/index.asp#FAQ06, May 1998. Last visited June 2007.

[6] Murad Muhammad Samir Muhammad Ali Abu Khalaf. Intelligent tracking of geostationary satellite systems. The university of Texas at Arlington, August 2000.

Appendix D

Hyperbolic derivation

D.1 Introduction

The following is the derivation of the field equations for the scattering across a hyperbolic reflector exited by a potter horn feed. It is an adaption of a similar derivation by *Rusch* [2].

D.2 Derivation

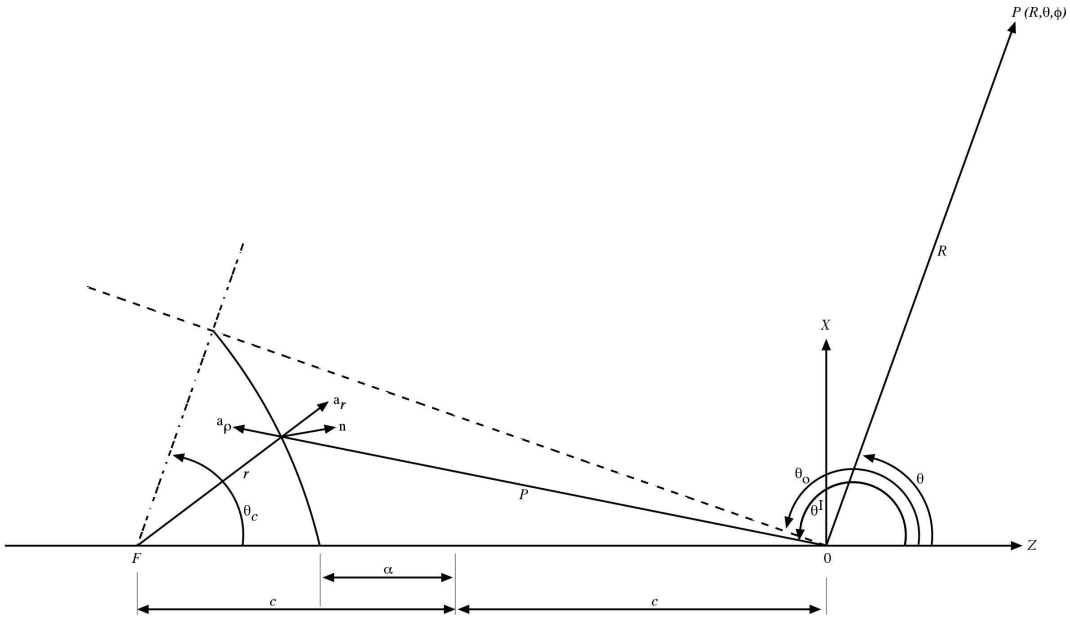


Figure D.1: Hyperbolic reflector orientation (adapted from work by *Rusch* [2]).

A potter horn feed is orientated at the origin O, facing the hyperbola - as shown in figure D.1. The reflected field in the $\mathbf{a}_r$ direction is given by *Silver* [3]:

$$\mathbf{E}_s(\theta,\phi) = \frac{-jw\mu}{2\pi R} e^{-jkR} \int_S \left(\mathbf{n}\times\mathbf{H}_i - \left(\left[\mathbf{n}\times\mathbf{H}_i\right]\cdot\mathbf{a}_r\right)\mathbf{a}_r\right) e^{jk\rho(\theta')\mathbf{a}_\rho\cdot\mathbf{a}_R} dS \tag{D.1}$$

Where:

n - unit normal vector to the hyperbolic surface.
$\mathbf{H}_i$ - magnetic field of the incident wave.

$\mathbf{a}_R$, $\mathbf{a}_\rho$ - unit vectors with reference to the Figure D.1

The pottern horn produces a wave propagating in the $\mathbf{a}_\rho$ direction of the form [1]:

$$\mathbf{E}_i = A_t P_t(\theta') \cos\phi' \mathbf{a}_\theta + A_p P_p(\theta') \sin\phi' \mathbf{a}_\phi \tag{D.2}$$

The magnetic field, $\mathbf{H}_i$ is thus:

$$\mathbf{H}_i = \left(\frac{\epsilon}{\mu}\right)(\mathbf{a}_\rho \times \mathbf{E}_i) \tag{D.3}$$

The expression $\mathbf{n} \times \mathbf{H}_i - (\left[\mathbf{n} \times \mathbf{H}_i\right] \cdot \mathbf{a}_r)\mathbf{a}_r$ is the condition that no current can flow out of the plane of the surface. The expression does not need to be explicitly calculated but rather by ignoring any transverse components in the expression $\mathbf{n} \times \mathbf{H}_i$. On reflection from the surface the coordinate system is rotated such that $\mathbf{a}_\rho \rightarrow \mathbf{a}_R$, $\mathbf{a}_{\theta'} \rightarrow \mathbf{a}_\theta$, $\mathbf{a}_{\phi'} \rightarrow \mathbf{a}_\phi$.
Substituting equation D.3 into $\mathbf{n} \times \mathbf{H}_i$ where:

$$\mathbf{n} = \frac{(1 + e\cos\theta')\mathbf{a}_\rho - e\sin\theta'\mathbf{a}_{\theta'}}{m(\theta')} \tag{D.4}$$

and,

$m(\theta) = [(1 + e\cos\theta')^2 + (e\sin\theta')^2]^{\frac{1}{2}}$
$e \equiv \frac{c}{a}$ for $(e > 1)$ (c and a defined in Figure D.1)

$$\begin{aligned}
\mathbf{n} \times \mathbf{H}_i &= \mathbf{n} \times \left(\frac{\epsilon}{\mu}\right)(\mathbf{a}_\rho \times \mathbf{E}_i) \\
&= \mathbf{n} \times \left(\sqrt{\frac{\epsilon}{\mu}} \begin{vmatrix} \mathbf{a}_\rho & \mathbf{a}_{\theta'} & \mathbf{a}_{\phi'} \\ 1 & 0 & 0 \\ 0 & A_t P_t(\theta')\cos\phi' & A_p P_p(\theta')\sin\phi' \end{vmatrix}\right) \\
&= \mathbf{n} \times \left(\sqrt{\frac{\epsilon}{\mu}}\right)\left(-A_p P_p(\theta')\sin\phi'\mathbf{a}_{\theta'} + A_t P_t(\theta')\cos\phi'\mathbf{a}_{\phi'}\right) \\
&= \frac{1}{m(\theta')}\sqrt{\frac{\epsilon}{\mu}} \begin{vmatrix} \mathbf{a}_R & \mathbf{a}_\theta & \mathbf{a}_\phi \\ (1 + e\cos\theta') & -e\sin\theta' & 0 \\ 0 & -A_p P_p(\theta')\sin\phi' & A_t P_t(\theta')\cos\phi' \end{vmatrix} \\
&= \frac{-1}{m(\theta')}\sqrt{\frac{\epsilon}{\mu}}(e\sin\theta' A_t P_t \cos\phi'\mathbf{a}_R + A_t P_t \cos\phi'(1 + e\cos\theta')\mathbf{a}_\theta \\
&\quad + A_p P_p(1 + e\cos\theta')\sin\phi'\mathbf{a}_\phi)
\end{aligned} \tag{D.5}$$

As no $\mathbf{a}_R$ component the equation simplifies to:

$$\begin{aligned}
[\mathbf{n} \times \mathbf{H}_i]_{Trans} = \frac{-1}{m(\theta')}\sqrt{\frac{\epsilon}{\mu}}(A_t P_t(\theta')\cos\phi'(1 + e\cos\theta')\mathbf{a}_\theta \\
+ A_p P_p(\theta')(1 + e\cos\theta')\sin\phi'\mathbf{a}_\phi)
\end{aligned} \tag{D.6}$$

Substituting equation D.6 into equation D.1:

$$\begin{aligned}
\mathbf{E}_s(\theta,\phi) = \frac{-jw\mu}{2\pi R}e^{-jkR}\int_S (\frac{-1}{m(\theta')}\sqrt{\frac{\epsilon}{\mu}}(A_t P_t(\theta')\cos\phi'(1 + e\cos\theta')\mathbf{a}_\theta \\
+ A_p P_p(\theta')(1 + e\cos\theta')\sin\phi'\mathbf{a}_\phi)e^{k\rho(\theta')\mathbf{a}_\rho \cdot \mathbf{a}_R} dS
\end{aligned} \tag{D.7}$$

From inspection $\mathbf{a}_\rho \cdot \mathbf{a}_R = \cos(\theta - \theta')\cos(\phi' - \phi)$ and dS is:

$$dS = \frac{-\rho(\theta')^2 \sin\theta' m(\theta') d\theta' d\phi'}{1 + e\cos\theta'} \tag{D.8}$$

Therefore:

$$\begin{aligned}\mathbf{E}_s(\theta,\phi) = \frac{-jw\sqrt{\epsilon\mu}}{2\pi R} e^{-jkR} \int_{\theta_0}^{\pi}\int_0^{2\pi} \big(A_t P_t(\theta')\cos\phi' \mathbf{a}_\theta \\ + A_p P_p(\theta')\sin\phi' \mathbf{a}_\phi\big)\rho^2(\theta')\sin\theta' \\ \times e^{k\rho(\theta')\cos(\theta-\theta')\cos(\phi'-\phi)} d\phi' d\theta\end{aligned} \tag{D.9}$$

Splitting into Components:

$$\begin{aligned}\mathbf{a}_\theta \cdot \mathbf{E}_s = \frac{-jw\sqrt{\epsilon\mu}}{2\pi R} e^{-jkR} \int_{\theta_0}^{\pi} A_t P_t(\theta')\rho^2(\theta')\sin\theta' \\ \int_0^{2\pi} \big(\cos\phi' e^{k\rho(\theta')\cos(\theta-\theta')\cos(\phi'-\phi)} d\phi' d\theta'\end{aligned} \tag{D.10}$$

$$\begin{aligned}\mathbf{a}_\phi \cdot \mathbf{E}_s = \frac{-jw\sqrt{\epsilon\mu}}{2\pi R} e^{-jkR} \int_{\theta_0}^{\pi} A_p P_p(\theta')\rho^2(\theta')\sin\theta' \\ \int_0^{2\pi} \sin\phi' e^{k\rho(\theta')\cos(\theta-\theta')\cos(\phi'-\phi)} d\phi' d\theta\end{aligned} \tag{D.11}$$

It is possible to simplify the $d\phi'$ integral using the expansion:

$$e^{j\psi\cos(\phi'-\phi)} = J_o(\psi) + 2\sum_{n=1}^{\infty}(j)^n J_n(\psi)\cos n(\phi' - \phi) \tag{D.12}$$

Where J_m is an m[th] order Bessel function. Consider only the $d\phi'$ integral of equation D.10 and substituting D.12, where $\psi = k\rho(\theta')\cos(\theta' - \theta)$:

$$\begin{aligned}&\int_0^{2\pi} \cos\phi' e^{k\rho(\theta')\cos(\theta-\theta')\cos(\phi'-\phi)} d\phi' \\ =\ & \int_0^{2\pi} \big(\cos\phi'\big[J_o(\psi) + 2\sum_{n=1}^{\infty}(j)^n J_n(\psi)\cos n(\phi'-\phi)\big]\big) d\phi' \\ =\ & J_o(\psi)\int_0^{2\pi}\cos\phi' d\phi' + 2\sum_{n=1}^{\infty}(j)^n J_n(\psi) \\ & \times \int_0^{2\pi}\cos\phi'\cos n(\phi'-\phi) d\phi' \\ =\ & 0 + 2\sum_{n=1}^{\infty}(j)^n J_n(\psi)\int_0^{2\pi}\big(\cos\phi'\cos n\phi'\cos n\phi + \cos\phi'\sin n\phi'\sin n\phi\big) d\phi'\end{aligned}$$

The case where $n = 1$ must be considered separately as it is underfined in the standard integral solution and

thus:

$$\begin{aligned}
&= 2jJ_1(\psi)\int_0^{2\pi}\left(\cos^2\phi'\cos\phi+\cos\phi'\sin\phi'\sin\phi\right)d\phi' \\
&\quad +2\sum_{n=2}^{\infty}(j)^nJ_n(\psi)\int_0^{2\pi}\left(\cos\phi'\cos n\phi'\cos n\phi+\cos\phi'\sin n\phi'\sin n\phi\right)d\phi' \\
&= 2jJ_1(\psi)\cos\phi\int_0^{2\pi}\cos^2\phi'd\phi'+2jJ_1(\psi)\sin\phi\int_0^{2\pi}\cos\phi'\sin\phi'\sin\phi d\phi' \\
&\quad +2\sum_{n=2}^{\infty}(j)^nJ_n(\psi)\left(\cos n\phi\left[\frac{\sin(1-n)\phi'}{2(1-n)}+\frac{\sin(1+n)\phi'}{2(1+n)}\right]_0^{2\pi}\right. \\
&\quad \left.+\sin n\phi\left[-\frac{\cos(n-1)\phi'}{2(n-1)}-\frac{\cos(1+n)\phi'}{2(1+n)}\right]_0^{2\pi}\right) \\
&= 2jJ_1(\psi)\cos\phi\pi+2jJ_1(\psi)\sin\phi\left[\frac{\sin^2\phi'}{2}\right]_0^{2\pi}=2\pi jJ_1(\psi)\cos\phi
\end{aligned} \tag{D.13}$$

Similarly for equation D.11

$$\int_0^{2\pi}\sin\phi' e^{k\rho(\theta')\cos(\theta-\theta')\cos(\phi'-\phi)}d\phi'=2\pi jJ_1(\psi)\sin\phi \tag{D.14}$$

Thus the integral simplifies to:

$$\mathbf{a}_\theta\cdot\mathbf{E}_s=\frac{w\sqrt{\epsilon\mu}}{R}e^{-jkR}\cos\phi\int_{\theta_0}^{\pi}A_tP_t(\theta')\rho^2(\theta')\sin\theta'J_1(\psi)d\theta' \tag{D.15}$$

$$\mathbf{a}_\phi\cdot\mathbf{E}_s=\frac{w\sqrt{\epsilon\mu}}{R}e^{-jkR}\sin\phi\int_{\theta_0}^{\pi}A_pP_p(\theta')\rho^2(\theta')\sin\theta'J_1(\psi)d\theta' \tag{D.16}$$

D.3 Conclusions

The derived field equations differ from those derived by *Rusch* [2] as they apply, specifically, for a potter horn feed case. Consequently they can be applied directly to the Hartebeesthoek Radio Astronomy Observatory's (HartRAO) 2.5 cm receiver system.

References

[1] Richard C. Johnson and Henry Jasik, editors. *Antenna Engineering Handbook*. McGraw-Hill Book Company, INC., second edition, 1984.

[2] W. V. T. Rusch. Scattering from a hyperboloidal reflector. Technical Report 32-283, Jet Propulsion Laboratory, July 1962.

[3] S. Silver. *Microwave Antenna Theory and Design*. McGraw-Hill Book Company, INC., 1949.

Appendix E

Reference Antenna Mounting

E.1 Introduction

Geostationary satellites orbit around the equator, an observer located on the equator could set up a polar mounted antenna to rotate in a single dimension and simplify source location. Observer latitude changes cause this straight line to be bent. By altering the angle of the hour angle mounted pole away from the usual latitude this arc can be flattened such that the observer can (if the antenna beam width is wide enough and the latitude is small enough) reduce searching to the simpler single dimension case.

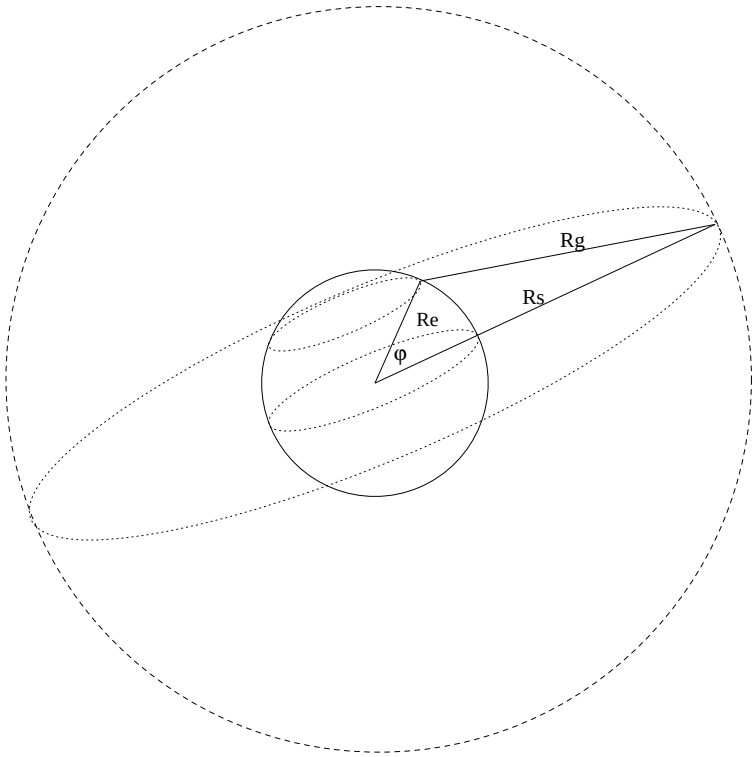


Figure E.1: Geometry of antenna and satellite showing the radius of the earth R_E, the radius of the satellite orbit R_S and its height above the observer R_g

E.2 Calculation

Firstly the look angles are calculated. The observer is located in spherical coordinates given by longitude λ,latitude φ and distance from the centre of the earth R_E. The Cartesian coordinates are calculated as:

$$\begin{aligned} X_A &= R_E \cos\lambda \cos\varphi \\ Y_A &= R_E \sin\lambda \cos\varphi \\ Z_A &= R_E \sin\varphi \end{aligned} \tag{E.1}$$

The satellite look angles (in hour angle α and declination δ) are calculated using the geometry shown in figure E.1. Satellite longitude λ_S and its distance from the earths centre R_S (for geostationary satellites are $(R_E + 35850)$ Km). The longitude is 0.

$$\alpha = -\arctan\left(\frac{R_S \sin(\lambda_S - \lambda)}{R_S \cos(\lambda_S - \lambda) - \sqrt{X_A^2 + Y_A^2}}\right) \tag{E.2}$$

$$\delta = -\arctan\left(\frac{Z_A}{\sqrt{R_S^2 + X_A^2 + Y_A^2 - 2R_S\sqrt{X_A^2 + Y_A^2}\cos(\lambda_S - \lambda)}}\right) \tag{E.3}$$

For HartRAO, located at the longitude $\lambda = +27\ 41'\ 07".107$ and latitude $\varphi = -25\ 53'\ 23".1246$ and a distance $R_E = 6375.5$ km from the earth's centre, $(X_A, Y_A, Z_A)_{\text{km}} = (5085.442, 2668.263, -2768.697)$. The calculated (α, δ) is plotted in figure E.2.

The affect on the look angles caused by rotating the antenna axis is calculated by rotating the unit

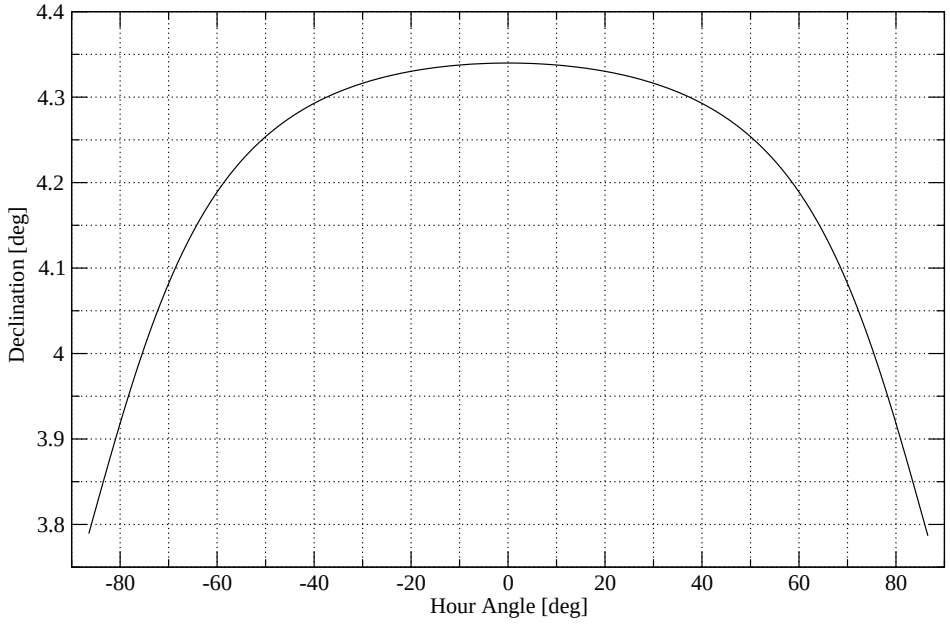


Figure E.2: Hour angle and declination satellite look angles calculated for the HartRAO telescope located at $(R_E, \lambda, \varphi) = (6375.5E3, 27.685, -25.890)$

vector matrix (X, Y, Z) to (X', Y', Z') below. The standard rotational matrices are used [1]. The antenna

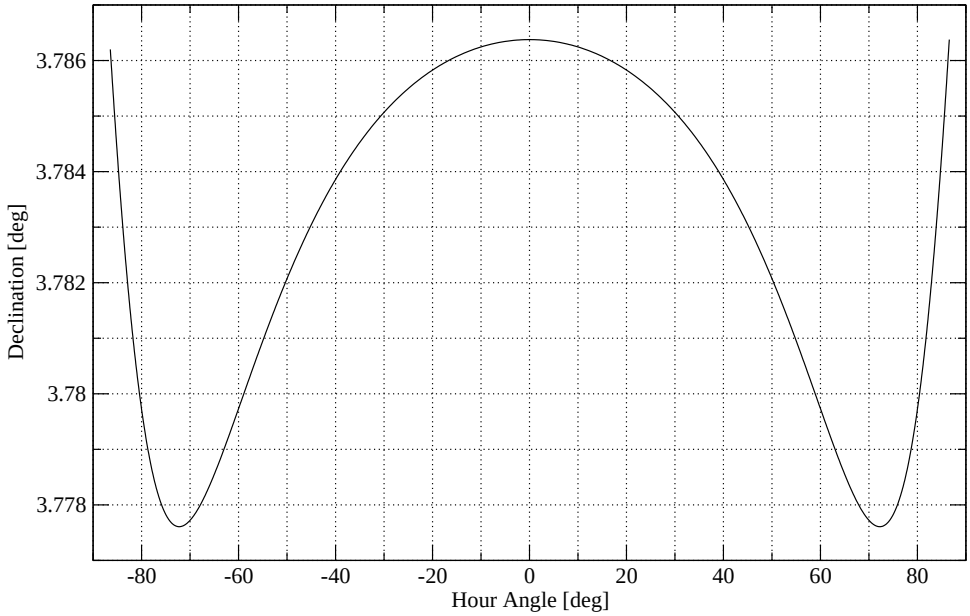


Figure E.3: Satellite look angles with tilted antenna

is tilted by an angle $\Delta\varphi$, so the coordinate system is rotated by $\varphi_{\mathrm{R}} = \varphi + \Delta\varphi$ from the horizontal.

$$\begin{aligned}
\begin{bmatrix} X' \\ Y' \\ Z' \end{bmatrix} &= \begin{bmatrix} X \\ Y \\ Z \end{bmatrix} R_y(\varphi_{\mathrm{R}} - 90) R_z(180) \\
&= \begin{bmatrix} X \\ Y \\ Z \end{bmatrix} \begin{pmatrix} \cos(\varphi_{\mathrm{R}} - 90) & 0 & -\sin(\varphi_{\mathrm{R}} - 90) \\ 0 & 1 & 0 \\ \sin(\varphi_{\mathrm{R}} - 90) & 0 & \cos(\varphi_{\mathrm{R}} - 90) \end{pmatrix} \\
&\quad \times \begin{pmatrix} \cos(180) & \sin(180) & 0 \\ -\sin(180) & \cos(180) & 0 \\ 0 & 0 & 1 \end{pmatrix} \\
&= \begin{bmatrix} X \\ Y \\ Z \end{bmatrix} \begin{pmatrix} \sin\varphi_{\mathrm{R}} & 0 & \cos\varphi_{\mathrm{R}} \\ 0 & 1 & 0 \\ -\cos\varphi_{\mathrm{R}} & 0 & \sin\varphi_{\mathrm{R}} \end{pmatrix} \begin{pmatrix} -1 & 0 & 0 \\ 0 & -1 & 0 \\ 0 & 0 & 1 \end{pmatrix} \\
&= \begin{bmatrix} X \\ Y \\ Z \end{bmatrix} \begin{pmatrix} -\sin\varphi_{\mathrm{R}} & 0 & -\cos\varphi_{\mathrm{R}} \\ 0 & -1 & 0 \\ \cos\varphi_{\mathrm{R}} & 0 & \sin\varphi_{\mathrm{R}} \end{pmatrix}
\end{aligned} \tag{E.4}$$

Substituting in (X, Y, Z),

$$\begin{aligned}
X' &= -\cos\delta\cos\alpha\sin\varphi_{\mathrm{R}} + \sin\varphi_{\mathrm{R}}\cos\varphi_{\mathrm{R}} \\
Y' &= -\cos\delta\sin\alpha \\
Z' &= \cos\delta\cos\alpha\cos\varphi_{\mathrm{R}} + \sin\delta\sin\varphi_{\mathrm{R}}
\end{aligned} \tag{E.5}$$

The solution of the optimal tilted angle is calculated numerical and for HartRAO the optimal value is 0.554° and the resulting look angles are plotted in figure E.3, the range of declination is reduced to 32 arc-seconds. For a standard satellite tracking antenna of half power beam width (HPBW) greater than 1° this allows for the antenna to be fixed at a single declination and track for satellites.

The rotated Azimuth and Elevation angles can be calculated using the standard calculation,

$$El = \arctan\frac{Z'}{\sqrt{X'^2 + Y'^2}} \tag{E.6}$$

$$Az = \arctan\frac{Y'}{X'} \tag{E.7}$$

The (Az, El) look angles are plotted in figure E.4. (It is clear that (Az, El) antennas cannot be configure in this way and this method is limited to (α, δ) antennas).

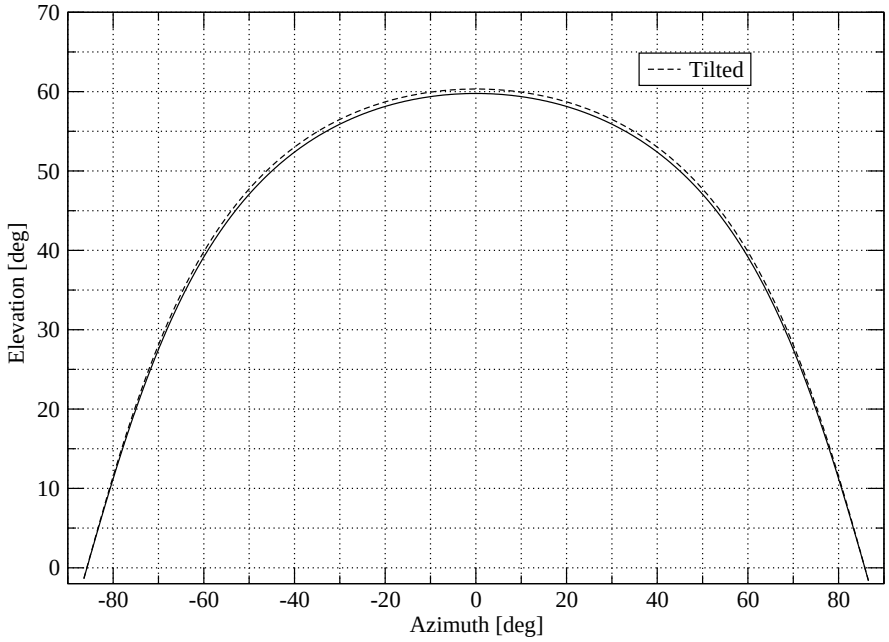


Figure E.4: Azimuth and elevation satellite look angles from HartRAO for tilted and standard axes.

E.3 Conclusions

By modifying the mount of the reference dish, for the HartRAO case, searching for geostationary satellites can be reduced to a single dimensional (and far simpler) case. The mathematics presented is general and can be applied with minor adjustment to any latitude. The method is constrained to a region (determined by the reference dish's HPBW) around the equator.

References

[1] Eric W Weisstein. Rotation matrix. From MathWorld–A Wolfram Web Resource. http://mathworld.wolfram.com/RotationMatrix.html. Last visited June 2007.